JOURNAL OF GEOPHYSICAL RESEARCH, VOL. 95, NO. B3, PAGES 2661-2678, MARCH 10, 1990

Melting in the Oceanic Upper Mantle: An Ion Microprobe Study of Diopsides in Abyssal Peridotites

KEVIN T. M. JOHNSON

MIT/Woods Hole Joint Program in Oceanography, Woods Hole, Massachusetts

HENRY J. B. DICK AND NOBUMICHI SHIMIZU

Woods Hole Oceanographic Institution, Woods Hole, Massachusetts

A systematic study of rare earth and other trace elements in discrete diopsides from residual abyssal peridotites sampled from 5000 km of ocean ridge demonstrates that they are the residues of variable degrees of melting in the garnet and spinel peridotite fields. Further, the data clearly demonstrate that the peridotites are the residues of near-fractional melting, not batch melting, and that typical abyssal basalt can evolve from aggregated fractional melts. Ion microprobe analyses of diopsides in abyssal peridotites from fracture zones along the America-Antarctica and Southwest Indian ridges reveal ubiquitous extreme fractionation of rare earth elements (REE) ($[Ce/Yb]_n$=0.002-0.05); depletion of Ti (300-1600 ppm), Zr (0.1-10 ppm), and Sr (0.1-10 ppm); and fractionation of Zr relative to Ti (Ti/Zr=250-4000). Ti and Zr in diopsides decrease with decreasing modal cpx in the peridotites, and samples dredged near hotspots are more depleted in incompatible elements than those dredged away from hotspots, consistent with higher degrees upper mantle melting in the former. All studied samples exhibit marked negative anomalies in Ti and Zr relative to REE. Incompatible element concentrations in peridotite clinopyroxenes are well modeled by repeated melting and segregation in ≤0.1% increments to a total of 5-25% melting, a process very close to Rayleigh (fractional) melting; batch melting of a LREE-depleted source cannot account for the observed trace element concentrations in abyssal peridotites. The shapes of some REE patterns are consistent with variable degrees of melting initiated within the garnet stability field. Trace element concentrations in calculated integrated fractional liquids approximate the composition of primitive ocean floor basalts, consistent with postsegregation aggregation of small increment melts produced over a depth and melting interval.

INTRODUCTION

Extensive geological and petrological evidence supports the contention that mid-ocean ridge basalts (MORB) are the products of decompression melting of a peridotitic mantle [*Green and Ringwood*, 1967; *Bottinga and Allègre*, 1978; *Ahern and Turcotte*, 1979; *Green et al.*, 1979; *le Pichon et al.*, 1982; *McKenzie*, 1984; *McKenzie and Bickle*, 1988], suggesting that the ocean crust should be underlain by a depleted residue of peridotite. Indeed peridotites have been dredged from numerous locations along the world ocean ridge system, and recent detailed mineralogic studies of these mantle peridotites have shown that they are the products of a large range of melting which increases systematically along the ocean ridges with proximity to postulated mantle hotspots [*Dick et al.*, 1984; *Michael and Bonatti*, 1985]. Moreover, the compositions of spatially associated abyssal basalts show complementary variations consistent with increasing depletion of the melt in magmaphile elements, particularly sodium, with increasing degree of mantle melting [*Dick et al.*, 1984; *Klein and Langmuir*, 1987]. This strongly supports the direct genetic relationship between abyssal peridotites and MORB inferred from plate tectonics and which has been inferred by numerous experimental studies of the basalt-peridotite system [e.g., *Mysen and Kushiro*, 1977; *Presnall et al.*, 1979; *Green et al.*, 1979; *Jaques and Green*, 1980; *Stolper*, 1980; *Takahashi and Kushiro*, 1983]. However, debate continues over whether mid-ocean ridge basalts sampled from the seafloor are primary melts formed at pressures between 8 and 11 kbar [*Presnall et al.*, 1979; *Takahashi and Kushiro*, 1983; *Fujii and Scarfe*, 1985; *Presnall and Hoover*, 1987] or are derivatives of higher-pressure (15-25 kbar) primary melts formed via polybaric crystal fractionation, mixing, and assimilation [*O'Hara*, 1968; *Green et al.*, 1979; *Stolper*, 1980; *Elthon and Scarfe*, 1984; *Falloon and Green*, 1987, 1988]. Most experimental studies compare compositions of experimentally produced liquids with natural MORB compositions, but studies focusing on the chemical characteristics of abyssal peridotites and their possible relations to MORB are scarce [e.g., *Shimizu and Hart*, 1974; *Dick et al*, 1984; *Michael and Bonatti*, 1985; *Shibata and Thompson*, 1986; *Johnson et al.*, 1987, 1988]. Defining and interpreting the chemical characteristics of abyssal peridotites, particularly with respect to the key incompatible elements, is therefore critical to understanding the evolution of the oceanic lithosphere.

Gradients in trace elements and isotopes in MORB from the Mid-Atlantic and Southwest Indian Ridge systems proximal to hotspots have been noted by several authors in studies of ocean floor basalts [*Hart et al.*, 1973; *Schilling*, 1975]. Incompatible elements become more enriched and variable in MORB near hotspots, reflecting a heterogeneous mantle source [*leRoex et al.*, 1983; 1989]. *Dick et al.* [1984] showed that abyssal peridotites and spatially associated basalts recovered from regions along the Mid-Atlantic, American-Antarctic, and Southwest Indian ridges conform to distinct melt extraction trends in several modal mineralogy and major element representations, and that abyssal peridotites recovered closest to hotspots are the most depleted in basaltic components. Hence it is expected that gradients in incompatible trace elements, reflecting greater degrees of melting and depletion near hotspots, should exist in abyssal peridotites in apparent contradiction to what is observed in many ridge basalts, which become enriched in incompatible trace elements approaching hotspots along-strike [*Schilling*, 1975].

Paper number 89JB03398.
0148-0227/90/89JB-03398$05.00

The trace element composition of the solid residues of melting is important not only for documenting the chemical composition of the mantle, but for describing the kind of melting which has occurred (e.g., fractional, incremental, dynamic, or batch melting). At low to intermediate degrees of melting, incompatible trace element concentrations in the residual solid phases will record the melting process better than the derived liquid will if the melts are mixed and homogenized in any way en route to the surface. Furthermore, if MORB are produced at a peritectic, then batch and fractional melting will produce melts of very similar major element compositions until a phase is lost.

Conversely, the composition of residual phases will evolve very differently in fractional and batch melting. Trace elements have been used to model melting in alpine peridotites [e.g., *Loubet et al.*, 1975; *Frey et al.*, 1985; *Prinzhofer and Allègre*, 1985] and also in modeling the evolution of derivative liquids in various mid-ocean ridge and oceanic island settings [e.g., *Gast*, 1968; *Langmuir et al.*, 1977; *Minster and Allègre*, 1978; *Hofmann and Feigenson*, 1983; *Bender et al.*, 1984; *Klein and Langmuir*, 1987]. However, because abyssal peridotites are scarce, pervasively serpentinized, and extremely depleted in incompatible elements, detailed geochemical studies of their bulk trace element compositions have heretofore not been undertaken. Compositions of unaltered minerals in the peridotites, however, provide reliable chemical information and can be used with confidence in constraining the magmatic processes affecting the rock as a whole. Since diopsides contain the highest concentrations of incompatible trace elements in typical oceanic peridotites (olivine + orthopyroxene + clinopyroxene + spinel), we have used the ion microprobe to analyze discrete diopsides in thin sections of serpentinized oceanic peridotites dredged from a 5000-km length of the American-Antarctic and Southwest Indian ridges (Figure 1). This contribution is the first to report incompatible trace element concentrations in abyssal peridotite clinopyroxenes collected by this method and to use these data to constrain melting processes in the mid-ocean ridge upper mantle.

Geological Setting and Samples

The abyssal peridotites in this study were dredged from fracture zones cutting the American-Antarctic and Southwest Indian Ridge systems. The American-Antarctic Ridge system extends from the Bouvet triple junction at 54°S, 1°W to the Scotia Arc at 60°S, 24°W, and separates the Antarctic plate to the south from the South American plate to the north (Figure 1). The half-spreading rate of this ridge is ~0.9 cm/yr [*Lawver and Dick*, 1983], lying at the slow end of the spreading rate spectrum for ocean ridges. Samples from the American-Antarctic Ridge dredged from the Vulcan (59°S, 18°W) and Bullard (57.5°S, 7.5°W to 58.5°S, 15.5°W) fracture zones during Leg 5 of the Vulcan expedition of the R/V *Melville* of Scripps Institution of Oceanography are designated Vulc 5-[dredge number]-[sample number].

The Southwest Indian Ridge system extends from the Bouvet triple junction northeastward to the Central Indian Ocean triple junction and separates the African plate to the north from the Antarctic plate to the south. It also has an extremely slow half spreading rate of ~0.86 cm/yr [*Sclater et al.*, 1976] and is characterized by short ridge segments offset by long fracture zones. Bouvet Island (Figure 1), situated in the southwestern rift mountains some 250 km east of the Bouvet triple junction, may be the surface expression of a hotspot [*Morgan*, 1972; *O'Nions and Pankhurst*, 1974]. Marion Island (Figure 1) may be the surface

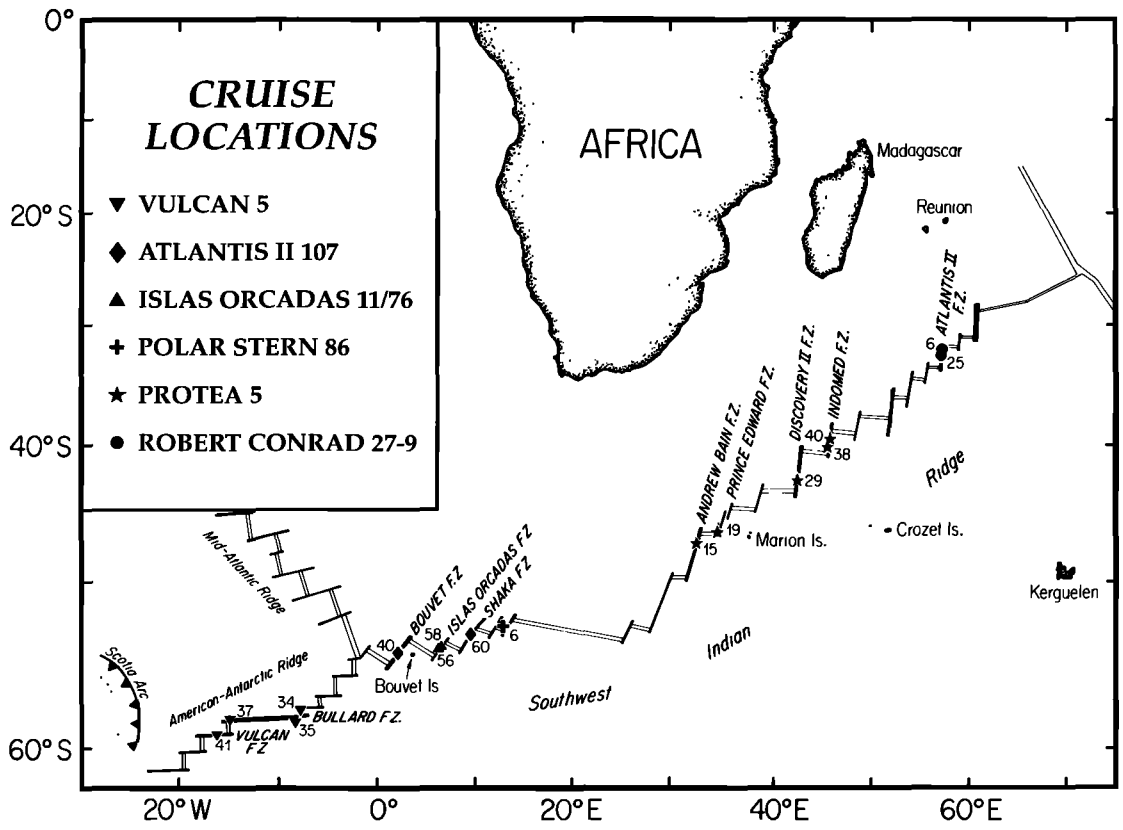

Fig. 1. Location map of American-Antarctica Ridge (AAR) and Southwest Indian Ridge (SWIR) showing dredge locations and locations of fracture zones, hotspots, and other features discussed in the text.

expression of another hotspot, based on shallow seafloor [*Fisher et al.*, 1987] and a positive residual geoid anomaly [*Rouffosse et al.*, 1981].

Samples from the southern portion of the ridge system are from Bouvet, Islas Orcadas, and Shaka fracture zones and the ridge-transform intersection east of the Shaka Fracture Zone and were dredged during cruise 107, leg 6 of the R/V *Atlantis II*, (AII107), cruise 11/76 of the R/V *Islas Orcadas* (IO11/76), and cruise 86 of the F/S *Polarstern* (PS86). Further to the north, samples were dredged from the Andrew Bain, Prince Edward, Discovery II, Indomed, and Atlantis II fracture zones during leg 5 of the Protea expedition of the R/V *Melville* (Prot 5), and cruise 27, leg 9 of the R/V *Robert Conrad* (RC27-9). All cruise designations are followed by -[dredge number]-[sample number]. Dredge locations and depth ranges are summarized in Table 1.

Abyssal peridotites are recovered in rift mountains and transform faults along the Atlantic and Indian Ocean ridges where the spreading rates are slow to very slow but are rare in dredge hauls from fast spreading ridges (a thorough discussion of their occurrence is given by *Dick* [1989]). Since they are probably emplaced at the base of the crust and faulted or otherwise uplifted to the surface, abyssal peridotites are the top of the mantle section, have experienced the greatest decompression, and likely represent the most extreme residues of the melting process in a given column.

Mineralogy

All samples in this study are plagioclase-free spinel peridotite tectonites with equigranular, protoclastic, or porphyroclastic textures. The primary phases are 65-82% modal forsteritic olivine (Fo_{89-92}), 12-25% enstatite ($Wo_{0.01-0.1}$), 2-12% diopside ($Wo_{0.45-0.5}$, $En_{0.45-0.48}$), and 1-3% Cr-Al spinel. The silicate phases are 20-100% replaced by serpentine or altered to clay minerals (Table 3). However, large parts of pyroxenes are frequently well-preserved and are suitable for chemical microanalysis.

Abyssal peridotites often contain plagioclase and hydrothermal alteration products such as chlorite, talc, tremolite, and hornblende occurring both in veins and as discrete reaction products. About a third of all dredged abyssal peridotites contain plagioclase. Only rarely is this phase found in more than trace amounts, though it is locally abundant at a few localities. In most locations, plagioclase is rare, occurring either interstitially to olivine and pyroxene, where it appears to be the product of late impregnation of the peridotite by basaltic melt [*Dick*, 1989] or occurring as exsolution blebs in aluminous pyroxene. It is extremely unlikely that plagioclase occurs as a residual phase (persisted throughout the course of melting) in any of the peridotites we have examined. In any event, samples that include hydrothermal minerals and plagioclase are excluded from this study because of their probable derivative nature.

Clinopyroxenes invariably exhibit some degree of orthopyroxene exsolution. Aside from inhomogeneity introduced by exsolution, grains appear to be unzoned. Based on backscattered electron images, exsolution in analyzed cpx was generally <10%, and exsolved grains were not recalculated to their primary compositions.

Analytical Techniques

The reported data are in situ analyses of diopsides and enstatites in thin sections of abyssal peridotites (Table 2). Major element data were collected on a JEOL 733 Superprobe at the Massachusetts Institute of Technology (MIT) using mineral standards and the Bence-Albee correction scheme. Accuracy and precision of major elements are $\pm\leq 1\%$ and minor elements are $\pm\leq 3\%$.

Samples were analyzed for rare earth elements and Ti, Sc, V, Cr, Sr, and Zr using the MIT-Brown-Harvard consortium Cameca IMS-3f ion microprobe at MIT For the major elements and relatively abundant trace elements, such as Sc, Ti, Cr, and V, a primary beam of negatively charged oxygen ions with a current of approximately 0.2 nA and a net energy of 12.55-12.65 keV

TABLE 1. Dredge Locations and Depths

Cruise and Dredge	Latitude	Longitude	Depth Range, m
Vulcan 5			
34, East Bullard FZ	57°46.9'S	7°40.3'W	3684-3983
35, East Bullard FZ	57°57.0'S	7°48.7'W	2920-3479
37, West Bullard FZ	58°25.8'S	15°39.7'W	3319-4104
41, Vulcan FZ	59°05.2'S	16°48.5'W	3379-4645
Atlantis II 107			
40, Bouvet FZ	54°25.3'S	1°31.7'E	2724-3240
60, Shaka FZ	53°27.3'S	9°10.0'E	4207-5349
Islas Orcadas 11/76			
56, Islas Orcadas FZ	54°05.5'S	6°17.1'E	3650-4390
58, Islas Orcadas FZ	54°04.3'S	6°23.9'E	2960-3580
PolarStern 86			
6, median valley, North wall	52°21.0'S	13°08.0'E	3073-3332
Protea 5			
15, Andrew Bain FZ	47°42.0'S	32°09.5'E	4000-4400
19, Prince Edward FZ	46°30.5'S	33°51.0'E	2700-3900
29, Discovery II FZ	42°41.1'S	41°53.7'E	4400-4600
38, Indomed FZ	39°47.3'S	45°59.3'E	1950-2125
40, Indomed FZ	39°43.1'S	46°17.7'E	2300-2800
Robert Conrad 27-9			
6, Atlantis II FZ	31°55.0'S	57°10.8'E	3500-3930
25, Atlantis II FZ	32°32.5'S	57°03.0'E	4745-5370

TABLE 2. Electron Microprobe Analyses of Pyroxenes in Abyssal Peridotites

Sample [a]	SiO_2	TiO_2	Al_2O_3	FeO	MnO	MgO	CaO	Na_2O	Cr_2O_3	Total	Ca	Mg	Fe	Mg #
Vulcan FZ														
Vulc5:41-15 (7)	50.46	0.49	8.20	3.01	0.08	14.95	21.09	1.15	0.99	100.41	0.477	0.470	0.053	0.899
Vulc5:41-30 (6)	50.66	0.31	5.68	2.73	0.06	15.76	22.57	0.45	0.99	99.21	0.485	0.470	0.046	0.911
Vulc5:41-30 (6)	54.42	0.09	4.18	6.16	0.06	32.67	1.03	0.01	0.58	99.20	0.020	0.887	0.094	0.904
Vulc5:41-33 (9)	51.50	0.25	5.30	2.75	0.07	16.43	21.86	0.42	0.92	99.50	0.466	0.488	0.046	0.914
Vulc5:41-45 (9)	50.42	0.39	6.40	2.88	0.07	15.67	22.86	0.42	1.05	100.16	0.488	0.465	0.048	0.906
Vulc5:41-45 (3)	54.09	0.09	5.08	6.70	0.11	32.89	0.79	0.00	0.63	100.38	0.015	0.884	0.101	0.897
Bullard FZ														
Vulc5:35-1 (4)	51.40	0.12	4.98	2.71	0.03	16.47	22.33	0.31	1.20	99.55	0.472	0.484	0.045	0.915
Bouvet FZ														
AII107:40-4 (7)	51.52	0.04	3.68	2.39	0.10	16.90	23.44	0.10	1.08	99.23	0.481	0.482	0.038	0.927
AII107:40-4 (3)	55.02	0.02	3.24	6.08	0.11	33.42	0.87	0.01	0.78	99.54	0.017	0.892	0.091	0.907
AII107:40-6 (15)	50.99	0.06	4.58	2.58	0.04	17.46	22.85	0.05	1.31	99.93	0.464	0.495	0.041	0.923
AII107:40-6 (5)	55.13	0.05	3.20	5.89	0.15	33.85	1.73	0.00	0.69	100.69	0.032	0.882	0.086	0.911
AII107:40-8 (10)	52.39	0.05	3.39	2.23	0.05	17.11	23.20	0.07	0.93	99.41	0.476	0.488	0.036	0.932
AII107:40-8 (4)	55.43	0.02	3.49	6.04	0.05	33.83	0.81	0.00	0.72	100.38	0.015	0.895	0.090	0.908
AII107:40-11 (6)	51.60	0.06	3.68	2.39	0.05	17.23	22.95	0.08	0.97	99.01	0.470	0.492	0.038	0.928
AII107:40-11 (3)	55.12	0.03	3.07	5.93	0.07	33.37	1.11	0.00	0.61	99.31	0.021	0.890	0.089	0.909
AII107:40-13 (9)	51.38	0.10	4.27	2.35	0.10	16.89	23.99	0.09	1.23	100.38	0.487	0.477	0.038	0.928
AII107:40-13 (5)	55.49	0.07	3.19	6.02	0.12	33.57	1.27	0.01	0.67	100.40	0.024	0.887	0.090	0.908
Islas Orcadas FZ														
IO11/76:56-57 (5)	50.68	0.27	5.56	2.15	0.08	15.93	23.22	0.62	0.94	99.42	0.494	0.471	0.036	0.929
IO11/76:56-57 (3)	53.11	0.05	5.98	7.15	0.03	31.73	0.95	0.05	0.70	99.74	0.019	0.871	0.110	0.887
IO11/76:58-18 (6)	50.75	0.22	5.89	2.28	0.05	15.43	23.35	0.51	1.11	99.58	0.501	0.461	0.038	0.923
IO11/76:58-18 (3)	53.90	0.06	5.04	6.25	0.10	32.69	0.89	0.05	0.69	99.67	0.017	0.887	0.095	0.903
IO11/76:58-34 (12)	51.34	0.15	5.80	2.28	0.08	15.41	22.93	0.64	1.06	99.67	0.497	0.465	0.039	0.923
IO11/76:58-34 (3)	53.71	0.02	5.81	6.89	0.17	31.92	0.51	0.00	0.84	99.87	0.010	0.883	0.107	0.892
Shaka FZ														
AII107:60-59 (3)	51.46	0.22	5.47	2.00	0.08	15.44	23.54	0.87	1.08	100.15	0.506	0.461	0.034	0.932
AII107:60-59 (3)	55.00	0.08	3.85	6.09	0.09	33.65	0.59	0.01	0.54	99.89	0.011	0.898	0.091	0.907
AII107:60-61 (6)	50.88	0.20	5.88	2.36	0.05	15.59	22.00	0.84	1.35	99.14	0.483	0.477	0.040	0.922
AII107:60-61 (3)	54.25	0.04	4.34	5.92	0.07	33.46	0.52	0.03	0.75	99.37	0.010	0.901	0.090	0.909
Andrew Bain FZ														
Prot5:15-90 (6)	50.40	0.20	5.75	2.85	0.07	16.28	22.03	0.33	1.34	99.24	0.470	0.483	0.048	0.910
Prot5:15-90 (3)	53.92	0.06	5.13	6.36	0.10	32.46	1.00	0.01	0.97	100.00	0.020	0.883	0.097	0.900
Prince Edward FZ														
Prot5:19-2 (15)	51.61	0.10	5.62	2.13	0.05	15.53	22.50	1.04	1.22	99.79	0.492	0.472	0.036	0.928
Prot5:19-2 (3)	54.53	0.00	5.07	5.74	0.11	33.12	0.63	0.05	0.82	100.05	0.012	0.900	0.087	0.911
Discovery II FZ														
Prot5:29-26 (15)	51.54	0.08	4.02	2.85	0.11	16.90	22.86	0.19	1.12	99.66	0.470	0.484	0.046	0.913
Prot5:29-26 (5)	55.33	0.07	3.35	5.99	0.15	32.54	1.91	0.00	0.84	100.16	0.037	0.873	0.090	0.906
Indomed FZ														
Prot5:38-1 (9)	51.81	0.11	5.27	2.51	0.07	16.34	22.04	0.52	1.17	99.82	0.472	0.487	0.042	0.921
Prot5:39-6 (9)	51.61	0.07	4.37	2.53	0.08	17.29	22.54	0.12	1.28	99.88	0.464	0.496	0.041	0.924
Prot5:40-88 (9)	51.51	0.11	3.94	2.13	0.08	16.31	24.16	0.14	1.42	99.77	0.498	0.468	0.035	0.931
Atlantis II FZ														
RC27-9:6-3 (6)	51.60	0.20	4.96	2.40	0.05	16.28	22.93	0.34	0.82	99.56	0.484	0.478	0.040	0.923

Values are in weight percent.

a - Numbers in parentheses are the number of points making up the average composition.

TABLE 3. Ion Microprobe Analyses of Clinopyroxenes in Abyssal Peridotites

Sample [a]	percent alter [b]	Mode [c] olivine	opx	cpx	spinel	Sc	Ti	V	Cr	Sr	Zr	Ce	Nd	Sm	Eu	Dy	Er	Yb
Vulcan FZ																		
Vulc5:41-13(5)	60	71.8	18.1	8.9	1.2	49	2615	279	5637	5.1	10.6	0.43	1.83	1.22	0.60	2.87	1.87	1.71
Vulc5:41-15(8)	60	63.9	22.7	12.0	1.4	49	2879	297	5925	5.4	11.5	0.50	1.92	1.24	0.57	2.56	1.79	1.61
Vulc5:41-30(3)	40	65.7	27.2	5.8	1.3	53	1979	309	7530	1.0	2.6	0.06	0.71	0.78	0.35	1.94	1.22	1.18
Vulc5:41-33(6)	40	68.1	21.0	9.9	1.0	54	1547	298	6759	2.1	5.0	0.17	0.60	0.70	0.32	1.78	1.14	1.18
Vulc5:41-45(7)	45	68.1	22.3	8.5	1.1	50	1554	355	7928	1.3	1.5	0.04	0.40	0.41	0.20	1.75	1.06	1.10
Bullard FZ																		
Vulc5:34-56(3)	80	74.8	17.1	7.5	0.6	64	796	274	7579	0.6	0.6	0.01	0.08	0.15	0.08	0.87	0.49	0.32
Vulc5:35-1(4)	25	74.4	19.2	6.0	0.4	70	754	300	7158	0.8	0.6	0.02	0.10	0.22	0.11	1.05	0.72	0.54
Vulc5:35-19(2)	30	70.0	22.1	6.9	1.1	56	1893	270	5876	3.1	4.5	0.33	0.61	0.50	0.21	1.71	1.01	0.74
Vulc5:35-22(4)	50	77.4	18.9	3.0	0.7	61	886	295	8150	1.8	0.3	0.01	0.04	0.12	0.07	0.82	0.64	0.57
Vulc5:35-30(8)	40	74.7	20.1	4.3	1.0	54	779	321	8955	3.8	0.3	0.02	0.12	0.17	0.09	1.16	0.79	0.89
Vulc5:37-3(2)	75	82.7	13.9	2.4	0.1	84	1335	367	8275	1.1	3.2	0.05	0.56	0.58	0.30	1.78	0.98	0.78
Bouvet FZ																		
AII107:40-6(5)	40	78.2	18.1	3.4	0.3	50	244	342	10227	1.2	0.1	0.01	0.02	0.05	0.02	0.55	0.46	0.57
AII107:40-8(6)	40	77.2	19.6	3.1	0.1	70	363	285	6534	0.7	0.1	0.04	0.13	0.08	0.04	0.48	0.50	0.63
AII107:40-11(9)	65	81.1	15.5	2.9	0.4	54	443	297	8392	0.5	0.1	0.01	0.02	0.05	0.03	0.70	0.57	0.70
AII107:40-13(5)	60	78.7	18.8	2.0	0.5	53	368	291	8519	1.2	0.1	0.01	0.01	0.05	0.03	0.38	0.43	0.46
AII107:40-27(5)	60	80.7	15.5	3.3	0.4	73	326	274	6518	0.8	0.2	0.02	0.04	0.07	0.03	0.52	0.52	0.53
Islas Orcadas FZ																		
IO11/76:56-57(4)	25	69.6	24.5	4.3	1.7	73	1608	301	6042	0.6	2.2	0.02	0.48	0.60	0.27	1.79	1.01	1.10
IO11/76:56-10(10)	20	73.4	18.7	7.2	0.7	44	1420	278	6925	0.6	1.4	0.02	0.47	0.48	0.30	2.12	1.57	1.57
IO11/76:56-54(4)	25	69.0	21.7	8.2	1.1	57	1606	276	7793	1.4	2.8	0.06	0.60	0.63	0.34	2.17	1.58	1.49
IO11/76:58-34(4)	25	70.0	25.9	3.5	0.6	52	1113	278	6053	20.2	1.1	1.55	0.60	0.34	0.18	1.46	1.01	0.69
East of Shaka FZ																		
PS86:6-37(3)		66.6	21.9	10.4	1.1	52	2674	293	6829	5.4	11.0	0.87	2.16	1.37	0.56	2.65	1.70	1.67
Andrew Bain FZ																		
Prot5:15-90(8)	20	70.0	22.0	7.0	1.0	41	1083	290	9462	0.4	0.5	0.02	0.24	0.39	0.18	1.18	0.69	0.74
Prince Edward FZ																		
Prot5:19-2(8)	5	72.9	23.4	3.1	0.6	78	598	258	7433	8.0	2.1	1.02	0.58	0.26	0.12	0.95	0.71	0.62
Discovery II FZ																		
Prot5:29-26(6)	40	63.5	28.6	7.0	0.9	74	527	276	7765	1.2	0.9	0.07	0.13	0.13	0.06	0.56	0.51	0.48
Indomed FZ																		
Prot5:38-1(3)	40	69.4	24.8	5.1	0.7	62	567	282	7124	0.6	0.4	0.03	0.12	0.15	0.08	1.02	0.74	0.54
Atlantis II FZ																		
RC27:9-6-3 (7)	35	67.1	25.6	6.6	0.6	55	1525	305	7051	1.2	2.1	0.04	0.47	0.62	0.33	1.93	1.17	0.78
RC27-9:6-8(8)	35	66.6	25.8	6.6	0.8	47	1702	338	6959	0.6	1.7	0.03	0.57	0.76	0.39	2.67	1.72	1.74
RC27-9:25-142(6)	40	56.1	33.5	9.0	1.5	38	1843	308	7334	1.2	3.1	0.11	0.91	0.92	0.47	2.40	1.50	1.63
Starting bulk mantle composition						1090					7.0	0.92	0.822	0.328	0.129	0.612	0.4	0.4
chondrite normalization values [d]						5.76	436	56.7	2650	7.91	3.94	0.616	0.457	0.149	0.056	0.245	0.16	0.159

Values in ppm.

[a] - Numbers in parentheses are number of cpx grains analyzed by ion probe in each sample. Each grain analysis is an average of up to three points, depending on grain size.

[b] - Reported alteration is mainly serpentinization but in a few cases includes clay minerals.

[c] - Modal analyses done by point counting ~2200-3000 points per thin section.

[d] - Chondrite normalizing values from *Anders and Ebihara* [1982].

was focused to a spot 5~8 μm in diameter. Positively charged secondary ions were mass analyzed by a double-focusing mass spectrometer with a high-energy offset of -90 eV and an energy bandpass of ±10 eV for a net secondary accelerating voltage of 4400-4420 eV (a technique known as energy filtering used to suppress molecular ion interferences [*Shimizu et al.*, 1978]) and were detected and counted by a 17-stage Allen type electron multiplier in pulse counting mode. For rare earth element (REE), Sr, Zr, and in some cases Ti, a primary beam with 1~2 nA current was focused to a spot of 12-20 μm. Energy filtering of -35 eV for REE and -90 eV for Ti, Sr, and Zr was used with an energy bandpass of ±10 eV. Empirical relationships between secondary ion intensities and concentration (working curves) were used to determine trace element concentrations. Sources of uncertainty include counting error, precision and accuracy of standard analyses used in constructing working curves, acquisition of mass peaks, and magnet drift. Overall accuracy and precision of the data (Table 3) are believed to be ±5~10% for Sc, Ti, Cr, and V; ±10~15% for Sr and Zr; ±10~20% for light REE; and ±10~15% for middle and heavy REE.

RESULTS

Modal clinopyroxene in the studied peridotites ranges from ~2 to ~12 vol % (Table 3) and is correlated with Ti and Zr (Figure 2). Clinopyroxenes are least abundant and most depleted in incompatible elements in peridotites closest to the Bouvet hotspot and have the highest Mg/(Mg+Fe) (Mg #) and among the lowest Ce concentrations (Figure 3), consistent with greater degrees of melting of the shallow mantle in these areas.

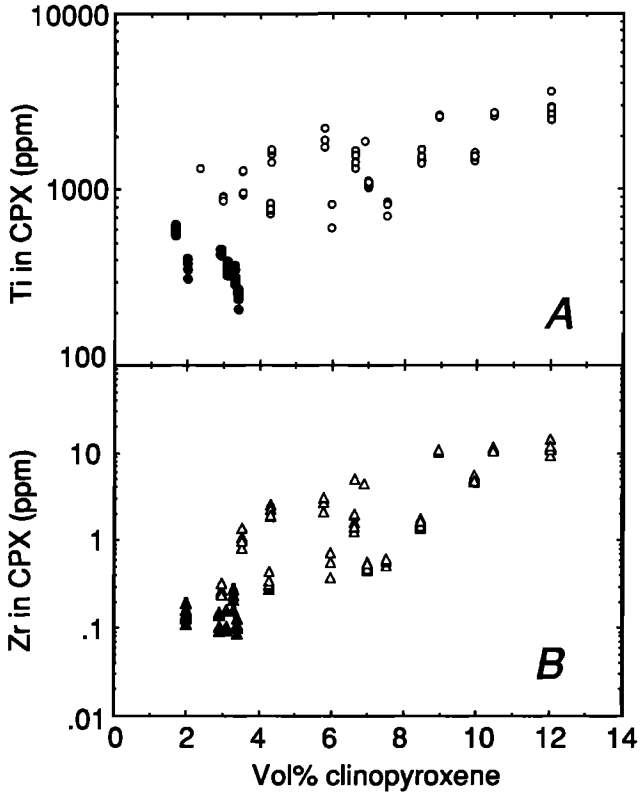

Fig. 2. Modal clinopyroxene in peridotite samples plotted versus (*a*) Ti, and (*b*) Zr in clinopyroxenes. Individual data points composing the averages reported in Table 3 are plotted. Clustering of points gives an indication of internal sample homogeneity. Solid symbols are those from the Bouvet FZ close to the Bouvet hotspot.

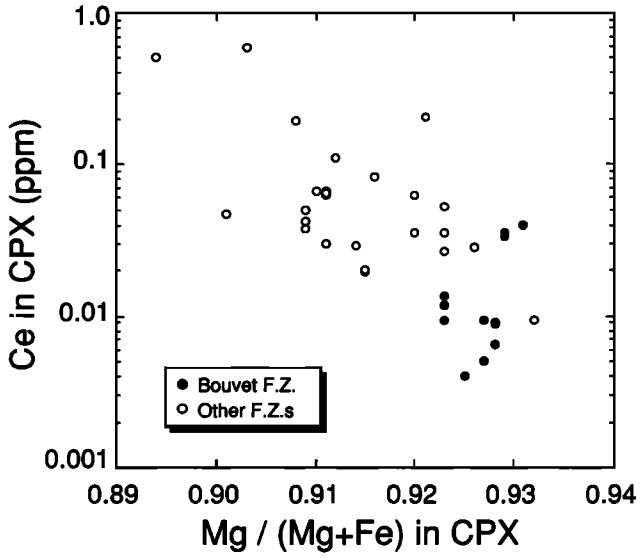

Fig. 3. Molar Mg/(Mg+Fe) (Mg #) versus Ce in peridotite clinopyroxenes. Depletion in Ce accompanied by an increase in Mg # is consistent with REE and Ti-Zr data and illustrates the residual nature of the samples and greater incompatible element depletion near the Bouvet hotspot. Solid symbols are data from the Bouvet Fracture Zone.

Incompatible element concentrations in peridotite clinopyroxenes range from 200 to 3500 ppm Ti, 0.4 to 8.0 ppm Sr, and 0.1 to 14.0 ppm Zr. The lowest incompatible element and highest compatible element concentrations invariably occur in samples nearest the Bouvet hotspot, as illustrated by concentration minima in the incompatible elements titanium, zirconium, dysprosium, and a concentration maximum in the compatible element scandium in clinopyroxene plotted as a function of distance from the Bouvet Hotspot (Figure 4). Though somewhat fewer data exist for the Marion hotspot region, the same relationship is suggested.

Most clinopyroxene REE patterns in this study are highly fractionated, but they differ between dredge hauls in their overall shape and degree of depletion. All analyzed samples from the Bouvet Fracture Zone near the Bouvet Hotspot exhibit steeply sloping light to middle REE (LREE-MREE) depleted patterns. These patterns are quite similar to those from the Discovery II Fracture Zone peridotites, dredged near the Marion Hotspot (Figure 5).

Clinopyroxenes from nonhotspot peridotites, on the other hand, generally exhibit steeply plunging LREE with flat to humped middle (MREE) to heavy rare earth elements (HREE) quite distinct from Bouvet and Discovery II FZ samples (Figure 6). Also plotted in Figure 6 are shaded fields representing hypothetical liquids in equilibrium with the peridotite clinopyroxenes, calculated using the partition coefficients listed in the appendix, and spatially associated MORB. The field for hypothetical liquids illustrates that most REE concentrations in clinopyroxene are inconsistent with simple clinopyroxene-MORB equilibrium.

Samples Prot 5: 19-2 from the Prince Edward Fracture Zone near the Marion hotspot and IO11/76: 58-34 from the Islas Orcadas Fracture Zone east of the Bouvet hotspot, exhibit LREE inflections in their REE patterns (Figure 7). Other samples from the same fracture zones do not show the same inflections, and we are analyzing other samples from the same dredge hauls to establish the scale of this geochemical anomaly.

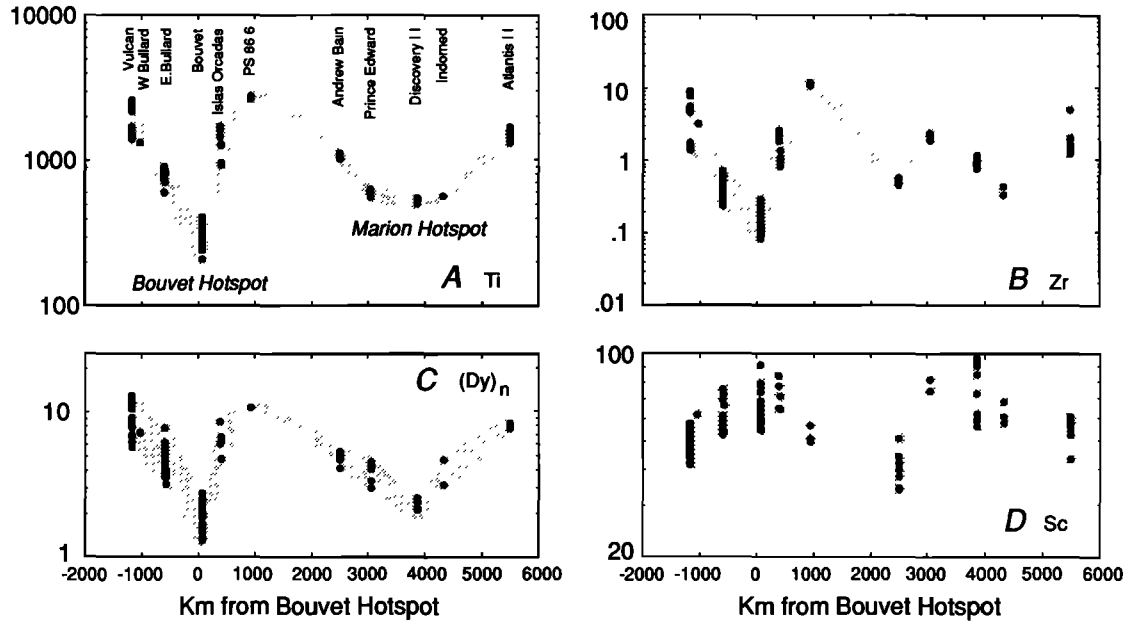

Fig. 4. Distance along the AAR and SWIR relative to the Bouvet hotspot versus (*a*) Ti, (*b*) Zr, (*c*) $(Dy)_n$, and (*d*) Sc in clinopyroxenes. Well-defined minima in incompatible elements Ti, Zr, and $(Dy)_n$ and a maximum in the compatible element Sc in the upper mantle diopsides nearest the two hotspots are evident.

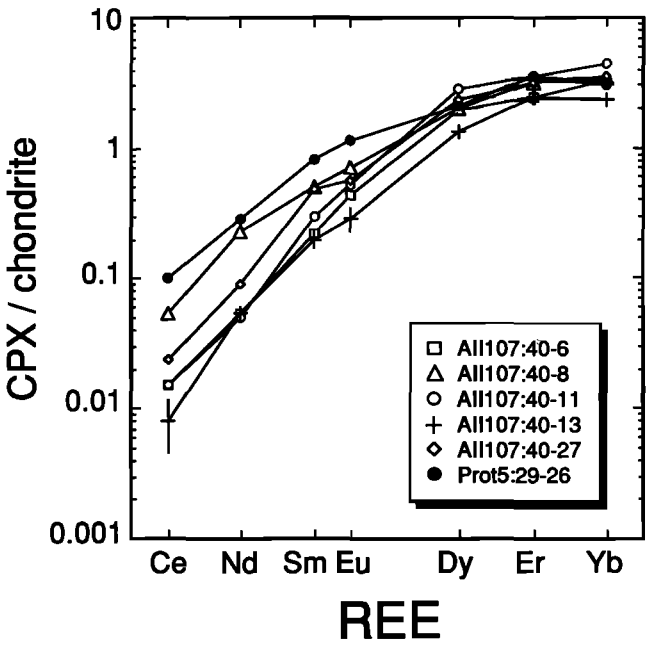

Fig. 5. Chondrite-normalized REE concentrations in diopsides from hotspot-proximal peridotites from Bouvet Fracture Zone (AII107) and Discovery II Fracture Zone (Prot 5). REE patterns in both locations have steeply sloping, LREE- depleted patterns unlike those from other sampled locations. Typical error bars are shown on AII107:40-13.

High field strength elements (HFSE), Ti and Zr, in peridotite clinopyroxenes are depleted relative to adjacent REE in incompatible element diagrams. These negative anomalies are illustrated by plotting Ti/Ti* versus Zr/Zr* (Figure 8), where Ti and Zr are chondrite normalized concentrations of those elements and Ti* and Zr* are calculated as $(Eu_n+Dy_n)/2$ and $(Nd_n+Sm_n)/2$, respectively [*Salters and Shimizu*, 1988]. Values less than 1.0 indicate negative anomalies, the smaller the value, the larger the anomaly. Primitive MORB (data from *Shibata et al.* [1979], *Sun et al.* [1979], *le Roex et al.* [1983], and *Humphris et al.* [1985]) cluster around 1.0, rarely exhibiting negative Zr anomalies but often exhibiting negative Ti anomalies (Figure 8). Zr/Zr* in clinopyroxenes from the Bouvet FZ peridotites are among the lowest (open circles in Figure 8), and those in samples from the Vulcan FZ range from relatively small anomalies in the less depleted samples, Vulc5: 41-13 and 41-15 (open triangles), to larger anomalies in the more depleted samples, Vulc5: 41-30 and 41-45 (solid triangles). HFSE depletions in mantle clinopyroxenes from a variety of geologic settings have been described [*Salters and Shimizu*, 1988], and it is now clear that these depletions are pervasive phenomena in the subridge oceanic upper mantle as well. This is an important observation because the major part of their data base is mantle xenoliths for which the provenance and petrogenetic evolution are generally unclear, whereas the geologic and tectonic setting of abyssal peridotites is well constrained.

In summary, the REE, Ti, and Zr data indicate that most of the studied abyssal peridotites could not have been in equilibrium with MORB. Furthermore, if MORB and abyssal peridotites are both descendents of pristine upper mantle lherzolite, they must be related by processes more complicated than simple equilibrium. In order to understand the process producing the extreme depletions of abyssal peridotites and to determine whether this process is capable of producing liquids with MORB compositions, forward melting models were computed.

Melting Models for Abyssal Peridotites

Melting equations relate incompatible element concentrations in residual solids and derived liquids to the type (e.g. Rayleigh [fractional], incremental, or batch) and degree of melting and can be used to test what type of melting abyssal peridotites have experienced and whether they are related to MORB by this melting process.

Peridotite clinopyroxenes were compared to models calculated from non-modal batch, incremental, and fractional

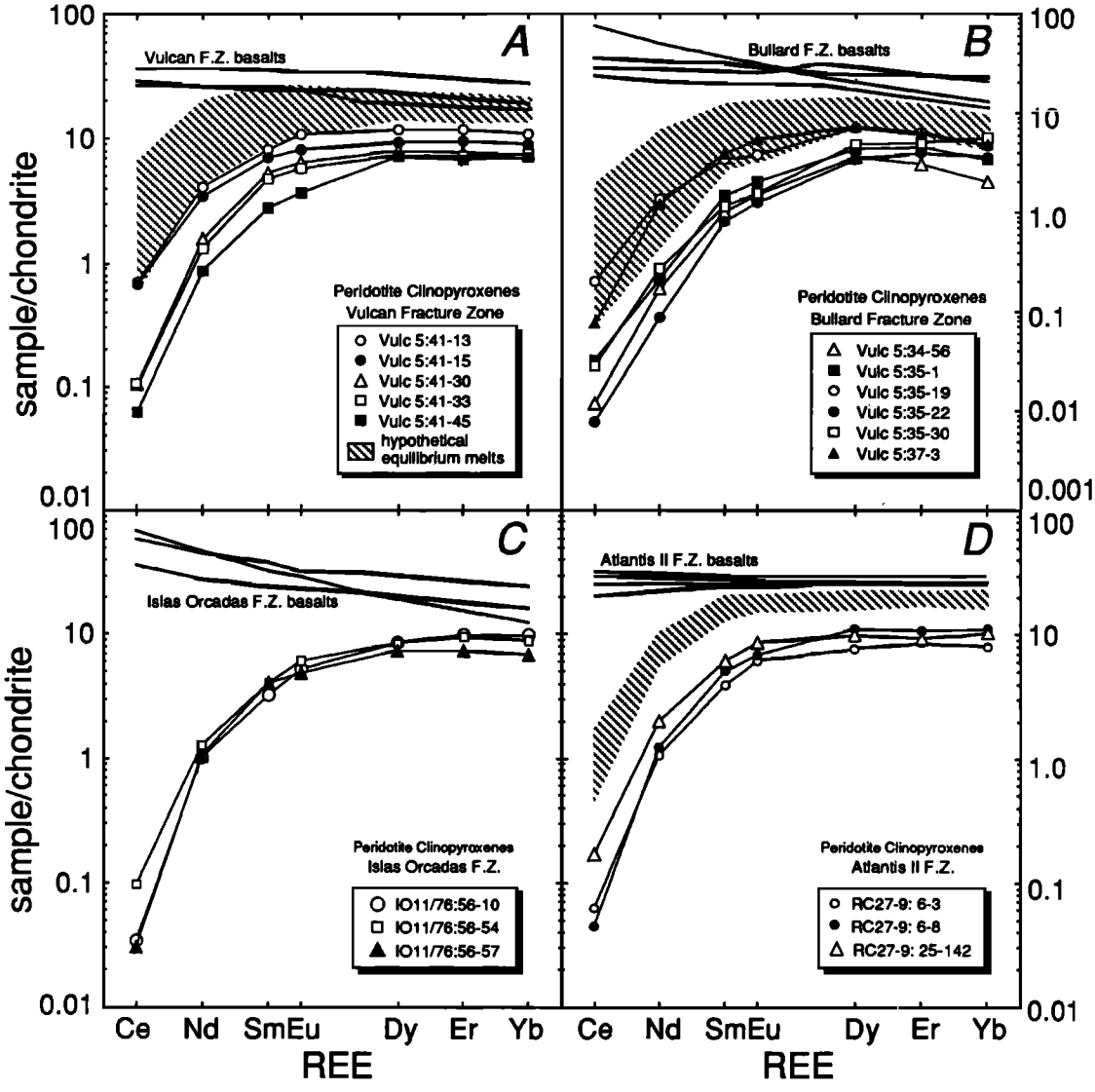

Fig. 6. Chondrite-normalized REE concentrations in nonhotspot peridotite clinopyroxenes. (*a*) Five samples from a single dredge haul in the Vulcan Fracture Zone on the AAR. Note flat HREE and sharp LREE depletions. (*b*) Six samples from three dredge hauls in East Bullard FZ (34 and 35) and West Bullard FZ (37). Note pronounced LREE depletions and hump at Dy (see text for detailed discussion). (*c*) three samples from the Islas Orcadas FZ, and (*d*) three samples from the Atlantis II FZ. Also shown are REE patterns in spatially associated basalts (data from *leRoex et al.* [1983, 1985] and K. Johnson, unpublished data, 1989) and fields representing hypothetical melts in equilibrium with the peridotite clinopyroxenes (cross-hatched).

melting equations derived from *Gast* [1968] and *Shaw* [1970, 1977]. In batch melting, solid and liquid fractions remain together throughout the entire melting interval, while in fractional melting infinitesimal increments of melting occur, accompanied by instantaneous segregation of the melt from the solid residue. Conceptually intermediate to these two theoretical end-members is incremental melting in which small, but finite, increments of melting and segregation occur, with a new starting composition employed after each segregation event. Equilibrium partitioning of elements is maintained in all models. Fractional melting depletes the residue in incompatible elements far more effectively than batch melting does and the two processes are easily distinguished in rare earth element diagrams and plots of incompatible elements in the residues [*Gast*, 1968]. Although compositions of infinitesimal fractions of melt produced by fractional melting are quite different from large batches of melt produced by batch melting, liquids produced by the two melting processes are virtually indistinguishable if fractional melts are integrated or aggregated following segregation from the source [*Shaw*, 1970].

Model element abundances in clinopyroxene in the residual solid were calculated to enable direct comparisons with the present data (see appendix for description of method). The partitioning behavior of Ti, Zr, and REE is reasonably well known, and these elements were used in forward modeling calculations. The important input parameters in the models are starting bulk composition, partition coefficients, proportions of minerals in the bulk solid, and those contributing to the liquid. The model starting bulk composition is a LREE-depleted lherzolite (1.5x to 2.5x C1 chondritic [*Loubet et al.*, 1975]), based on Nd and Hf isotope compositions of MORB. The starting bulk composition is listed in Table 3, and all modeling calculations and results are reported in terms of cpx in the residue. Mineral melting proportions were taken to be those

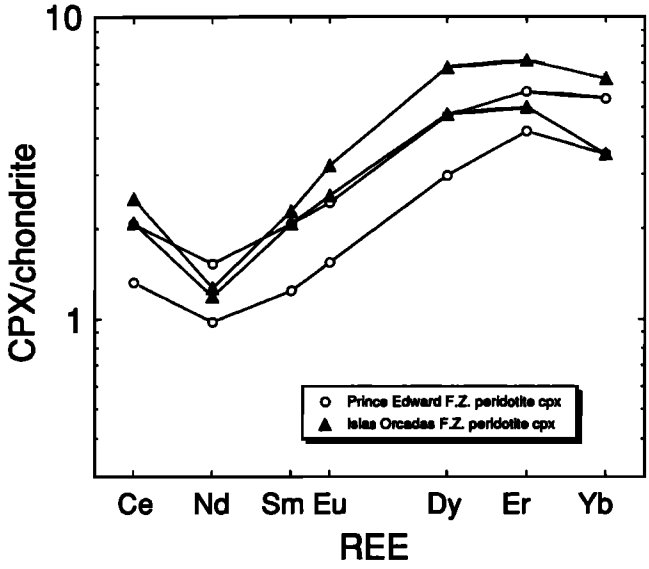

Fig. 7. Chondrite-normalized REE concentrations in individual peridotite clinopyroxenes from Prot 5:19-2 (Prince Edward FZ) and IO11/76:58-34 (Islas Orcadas FZ) showing positive LREE anomalies. Similar inflections were theoretically modeled for early stages of metasomatism of a depleted mantle [*Navon and Stolper*, 1987].

comprising peritectic melts in a four-phase peridotite assemblage and calculations were carried to 25% melting, prior to the elimination of cpx in the modeled peridotite assemblages (the Bouvet and Discovery II FZ samples are modeled differently as discussed below). Starting mineral proportions are listed in the appendix.

Partition Coefficients

Partition coefficients used in the calculations are listed in the Appendix. Most of our chosen partitioning data for clinopyroxene and garnet are from experiments since intensive parameters can be controlled and equilibrium can be assessed. Coefficients were obtained from doped experiments that observe Henry's law behavior [*Grutzeck et al.*, 1974; *McCallum and Charrette*, 1978; *Terakado and Masuda*, 1979; *Nicholls and Harris*, 1980], experiments at natural concentration levels analyzed by isotope dilution, neutron activation, or X ray fluorescence of separated phases [*Shimizu and Kushiro*, 1975; *Fujimaki et al.*, 1984], or by ion or proton microprobes [*Green et al.*, 1989; *Johnson and Kinzler*, 1989]. Partitioning data for other phases in peridotites are taken from *Stosch* [1982], who measured $D_{REE}^{cpx/liq}$ in a large number of mantle xenoliths.

Despite the large number of studies on cpx/liquid partitioning, uncertainties still exist concerning the effects of pressure on partitioning behavior. While some studies report little or no pressure effect on $D_{REE}^{cpx/liq}$ (e.g., *Fujimaki et al.* [1984] and *Colson and Gust* [1989], low-Ca pyroxene), others report an increase in $D_{REE}^{cpx/liq}$ with increasing pressure [e.g., *Green and Pearson*, 1985]. Although moderate to high pressure partition coefficients [*Green and Pearson*, 1985; *Johnson and Kinzler*, 1989] are close to those determined from megacryst/host pairs [e.g., *Irving and Frey*, 1984], the "pressure" effect is unresolved. Partition coefficients used in the calculations are summarized in the appendix.

Model Results and Discussion

Ti and Zr concentrations in peridotite clinopyroxenes and in basalts from nearby ridge segments are plotted in Figures 9*a* and 9*b*, respectively. The wide concentration range and progressive increase in Ti/Zr with decreasing concentrations in the peridotite clinopyroxenes is evident. Spatially associated MORB range from 3500 to 15,000 ppm Ti, 70 to 200 ppm Sr, and 40 to 200 ppm Zr. Assuming cpx/basaltic liquid partition coefficients of 0.35-0.49, 0.1, and 0.14-0.21 for Ti, Sr, and Zr, respectively [*Ray et al.*, 1983; *Fujimaki et al.*, 1984; *Dunn*, 1987;

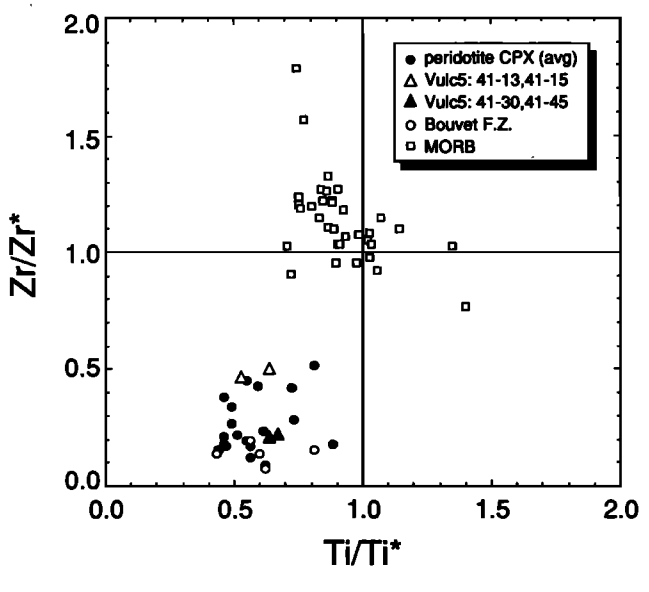

Fig. 8. Ti/Ti* versus Zr/Zr* calculated according to the procedure discussed in the text. Data points are sample averages and illustrate the ubiquitous negative HFSE anomalies relative to adjacent REE in clinopyroxenes in a typical incompatible element diagram sequence. Open circles are Bouvet FZ samples and triangles are Vulcan FZ samples. Primitive MORB data from *Shibata et al.* [1979], *Sun et al.* [1979], *Humphris et al.* [1985], and *leRoex et al.* [1983]. See text for discussion.

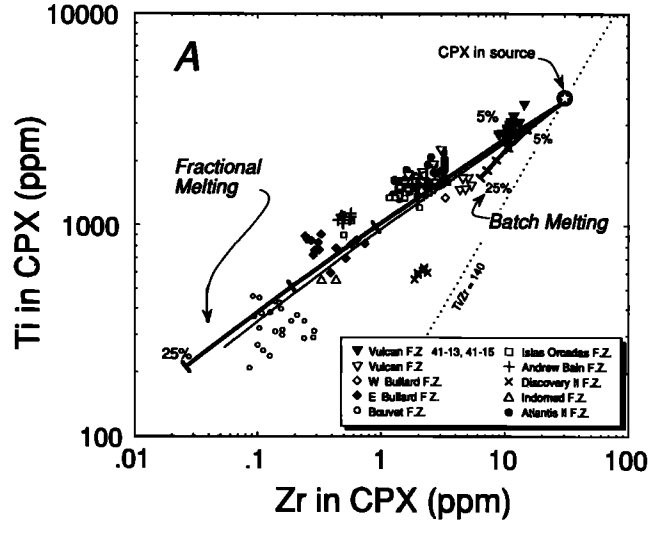

Fig. 9*a*. Ti and Zr concentrations in peridotite clinopyroxenes. Also shown are model melting curves calculated using the procedure discussed in the text and appendix. The fine line subparallel to the fractional melting trend is the model for melting and segregation in 0.1% increments. Clinopyroxene data conform more closely to the model trend for the residue of fractional or incremental melting than to the batch melting trend. Ticks are at 5% intervals and refer to the total degree of partial melting. Also shown is a line for Ti/Zr = 140 to illustrate the efficiency of fractional melting and inefficiency of batch melting and fractional crystallization in changing this ratio.

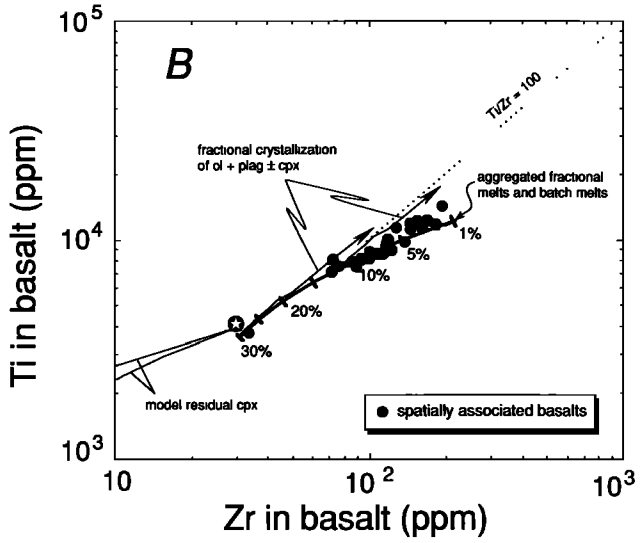

Fig. 9*b*. Ti and Zr concentrations in basalts spatially associated with the studied peridotites. Model liquid curves for integrated or aggregated fractional melts and for fractional crystallization of these melts show that the full range of data can be produced by the combination of fractional melting, aggregation, and fractional crystallization. The curve for batch melts is not shown, but virtually coincides with that for aggregated fractional melts. Also shown is a line for Ti/Zr = 100 which is a near-chondritic value and is relatively constant in MORB. Data from *leRoex et al.* [1983, 1985].

Tormey et al., 1987; *Johnson and Kinzler,* 1989], hypothetical equilibrium liquid concentrations of 550-10,000 ppm Ti (0.09-1.7 wt %), 2.0-60 ppm Sr, and 0.7-100 ppm Zr are implied. Basaltic liquids with compositions near the upper end of these hypothetical ranges occur, but we are not aware of any basaltic liquids recovered from the ocean basins with compositions even approaching the lower end of the ranges.

Also plotted in Figure 9 are model melting curves calculated from the melting equations in the appendix and for melting in 0.1% increments (fine line subparallel to the fractional melting curve). The model starting composition (Table 3) was chosen to be consistent with a light REE depleted chondritic source. It is immediately evident that the broad range in Ti and Zr concentrations in the peridotite clinopyroxenes can not be achieved by batch melting to any reasonable degree (short curve in Figure 9*a*). Ti/Zr ranges from 250 in the least depleted clinopyroxene to 4000 in the most depleted, a change that can be produced by an additional ~18% fractional melting or ~20% incremental melting but cannot be produced by any amount of batch melting, as evidenced by only a minor deviation of the batch melting curve from the starting cpx Ti/Zr ratio of 140. The most depleted samples (Bouvet Fracture Zone) are consistent with a total of 20-25% fractional or incremental melting, the remainder of the samples ranging upward in concentration consistent with lower degrees of melting. This agrees well with the total range in melting predicted using the lever rule and the overall variation of modal mineralogy in these samples by *Dick et al.* [1984] providing model independent confirmation of the result. Samples Vulc 5: 41-13 and 41-15 are more enriched in Ti and Zr than other samples analyzed (Figure 9*a*), and it is not possible to determine whether they have formed by batch or fractional melting using the Ti-Zr model. However, it will be shown below that REE can better discriminate between melting processes responsible for producing these less depleted compositions.

Melts produced by the above model calculations are compared to ocean floor basalt compositions in the studied areas (Figure 9*b*). The curved line is the integrated fractional melt composition at various degrees of melting. The composition of melts produced by batch melting define a line essentially coincident with the aggregated fractional melt line and are not shown for diagrammatic clarity. Arrows emanating from the melting curve are paths the liquid would follow during fractional crystallization of olivine + plagioclase ± clinopyroxene. Three points can be made from these diagrams: (1) Residual clinopyroxene compositions plot very close to the fractional melting end-member model, (2) Fractional melting, aggregation, and fractional crystallization are capable of producing the array of MORB found in the area where the peridotites were dredged, and (3) if melts are pooled, or otherwise aggregated prior to eruption, then MORB compositions are ineffective in deducing the melting process by which they formed.

Two end-member forward melting models were computed for REE as they were for Ti-Zr. The results are summarized as follows:

1. The extreme fractionation of REE observed in the data was never achieved by any degree of batch melting using reasonable starting compositions, mineral assemblages, or sets of $D_{REE}^{cpx/liq}$ (Figure 10*a*).

2. Fractional melting or incremental melting of very small (≤ 0.1%) increments totaling up to 10% melting in the spinel field alone produce model patterns with flat HREE consistent with data from Vulcan FZ (Figures 10*b* and 10*c*), Islas Orcadas FZ, and Atlantis II FZ (Figure 11). REE in integrated fractional liquids also resemble spatially associated MORB (Figure 10*d*). The results of the fractional and 0.1% incremental models differ only slightly from one another, as expected, and total degrees of melting for the Vulcan FZ samples deduced from REE modeling agree well with the values obtained from Ti-Zr modeling. Samples Vulc5: 41-13 and 41-15 are consistent with ≤5% fractional or incremental melting but not with batch melting, eliminating the ambiguity over the melting process noted above in the Ti-Zr modeling results.

3. Samples from Bouvet and Discovery II fracture zones, which are near hotspots, have distinct REE patterns (Figure 5) that are difficult to model by simple melting of four-phase peridotite assemblages. The major difficulty is that although the REE data are fractionated, they are not flat or humped in the MREE to HREE but are steeply inclined from HREE to LREE. Although the unusual patterns might reflect different source compositions from the other studied areas, the similarity of REE patterns in samples from the Bouvet and Discovery II fracture zones, both adjacent to hotspots but separated by several thousand kilometers, implies that the REE traits might be process related. To investigate this possibility, we constructed a multistage model involving the following steps: (1) relatively high degrees of melting in the garnet stability field leaving residual garnet, (2) decompression reaction of garnet to form 2 pyroxenes + spinel, and (3) continued melting in the spinel stability field and granule exsolution of cpx from opx.

If melting in the garnet stability field consumes most of the primary clinopyroxene, and decomposition of the residual garnet due to decompression into the spinel field produces clinopyroxene by the reaction:

$$Mg_2SiO_4\ (Ol) + Ca_{0.75}Mg_{2.25}Al_2Si_3O_{12}\ (Gt) = 2.5MgSiO_3\ (En) + MgAl_2O_4\ (Sp) + 0.75CaMgSi_2O_6\ (Di) \quad (1)$$

Clinopyroxene produced by this reaction would inherit the

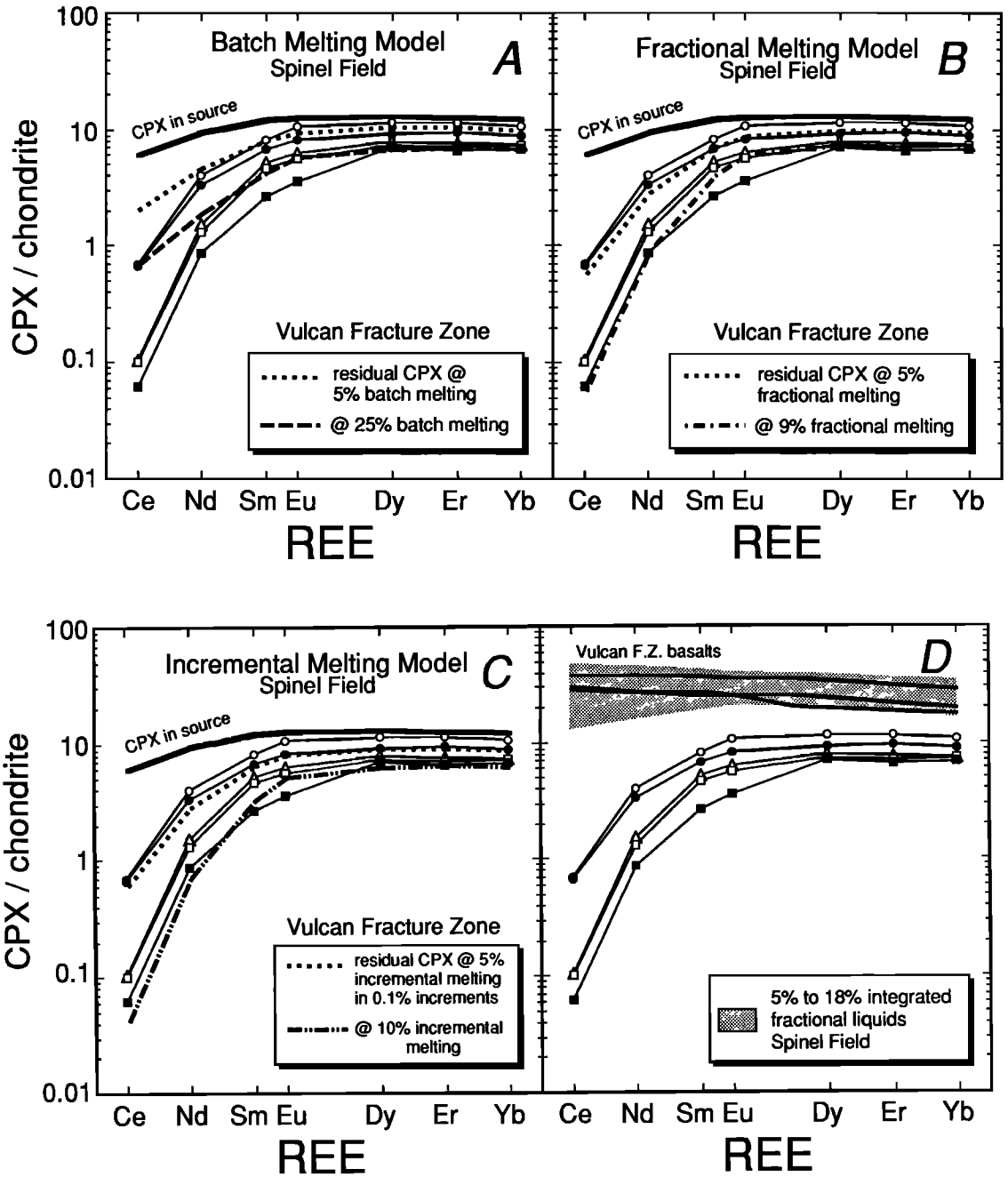

Fig. 10. (*a*) Model batch melting residues of a depleted, 2.5x chondritic source calculated for a spinel peridotite assemblage (dashed lines) compared to REE data from Vulcan FZ peridotite clinopyroxenes showing that LREE depletions in the samples are too extreme to be modeled by batch melting. (*b*) The same data plotted with model fractional melting residues and (*c*) Residues formed by repeated melting and segregation of 0.1% melt increments to 5-10% total melting show good agreement with peridotite clinopyroxenes. (*d*) The field for 5-18% integrated fractional liquids plotted with spatially associated basalts (data from *leRoex et al.* [1985]). Symbols as in Figure 6.

general shape of the garnet REE pattern, mitigated by interphase partitioning, but further melting of the residual lherzolite in the spinel stability field after recrystallization produces residual cpx with REE patterns that are more fractionated than the data.

Lindsley and Andersen [1983] showed that under cooling conditions similar to those assumed for the upper mantle-crust, orthopyroxene can exsolve up to 9 wt % clinopyroxene, a figure that is consistent with our observations of exsolution lamellae in some samples. At relatively high temperatures where diffusion is sufficiently rapid, some portion of the exsolution lamellae may coalesce into discrete cpx grains in a process known as "granule exsolution" [*Lindsley and Andersen*, 1983]. Assuming that of the total exsolution in a sample no more than 50% granule exsolution results, a few weight percent of secondary (or tertiary) cpx may be formed. Using this model and the parameters stated in the appendix, we were able to approximate the shape of the hotspot-related peridotite clinopyroxene patterns (Figure 12).

4. REE patterns of clinopyroxenes in samples from the Bullard FZ display humps at the middle to heavy REE (Dy-Er) and

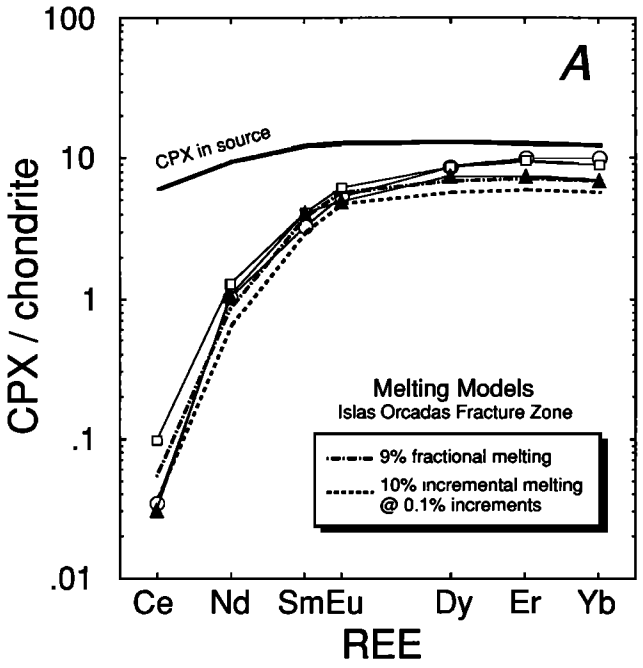

Fig. 11*a*. Melting models for samples from the Islas Orcadas FZ calculated as in Figure 10 to illustrate the probable limits of fractional or incremental melting experienced. Symbols as in Figure 6.

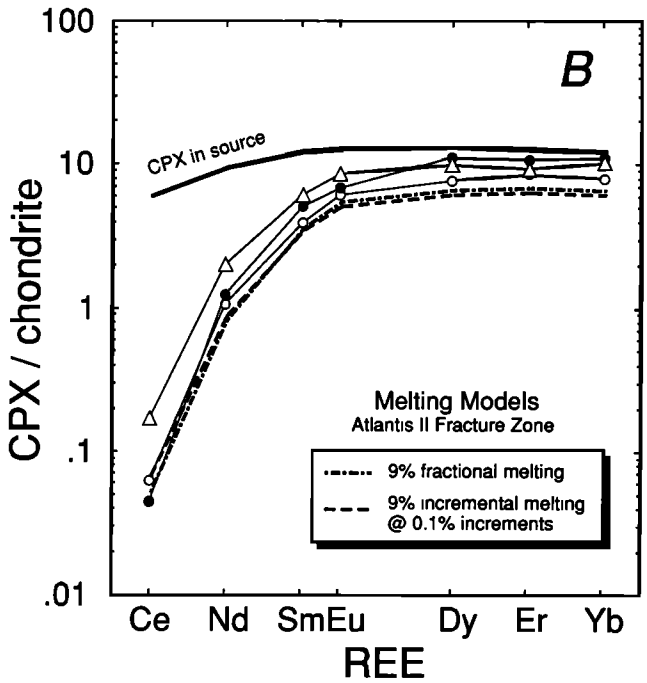

Fig. 11*b*. Melting models for samples from the Atlantis II FZ calculated as in Figure 10 to illustrate the probable limits of fractional or incremental melting experienced. Symbols as in Figure 6.

cannot be modeled by melting in the spinel stability field alone using the same starting conditions and model parameters as in the Vulcan FZ modeling. However, when garnet lherzolite is used as the starting composition in the early stages of melting, model residual clinopyroxene compositions develop humps at the MREE to HREE (Figure 13). Modeling results show that fractional melting or ≤0.1% melting increments totaling 8-10% in

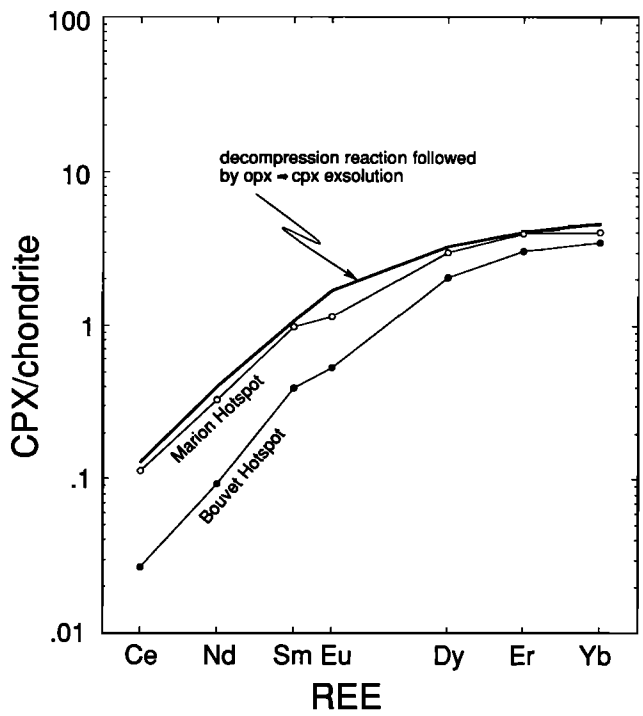

Fig. 12. Model to explain the REE patterns observed in Bouvet FZ and Discovery II FZ peridotite clinopyroxenes calculated according to the scheme explained in the text for a multistage melting and exsolution process. Using the starting parameters in the appendix, melting starting in the garnet stability field leaving some residual garnet, followed by the reaction garnet = 2 px + spinel and cpx granule exsolution from opx can produce cpx with the REE pattern shown. The curves are averages of data presented in Figure 5.

the garnet stability field, followed by an additional 1-10% (total) fractional or incremental melting in the spinel stability field fit the data quite well.

It was found that using garnet in the melting assemblage for the Ti-Zr model did not significantly change the trajectory of the model melting curves, though it did shorten them somewhat. This means that the apparent degree of melting inferred from Figure 9*a* for samples from the Bullard, Bouvet, and Discovery II FZs, which were modeled using garnet, would be slightly higher. However, since we feel that the partiton coefficients for Ti and Zr in garnet are less well known than those for cpx, we decided not to include garnet model curves in Figure 9*a* since no quantitatively definitive improvement of the curves was achieved.

The degree of REE fractionation and development of the MREE hump are functions not only of the partition coefficients used in the model but also of the phase proportions both in the bulk solid and contributing to the melt phase. Variations in depth of melting within the garnet stability field will control the position of the garnet-cpx eutectic [*Davis and Shairer*, 1965; *O'Hara and Yoder*, 1967] and consequently control the proportions of phases entering the melt ($p\alpha$). We used two different melting phase proportions in our models to determine the effect this has on clinopyroxene patterns and the result is shown in Figure 13. Model REE patterns calculated with p_{cpx}:p_{garnet} = 0.44:0.50 (higher pressures) develop more pronounced MREE humps at similar degrees of melting than patterns produced by p_{cpx}:p_{garnet} = 0.25:0.5 (lower pressures). The lightly stippled field in Figure 13 is calculated using p_{cpx}:p_{garnet} = 0.44:0.50 and the heavy, dashed line is calculated with p_{cpx}:p_{garnet} = 0.25:0.5. Integrated fractional liquids define

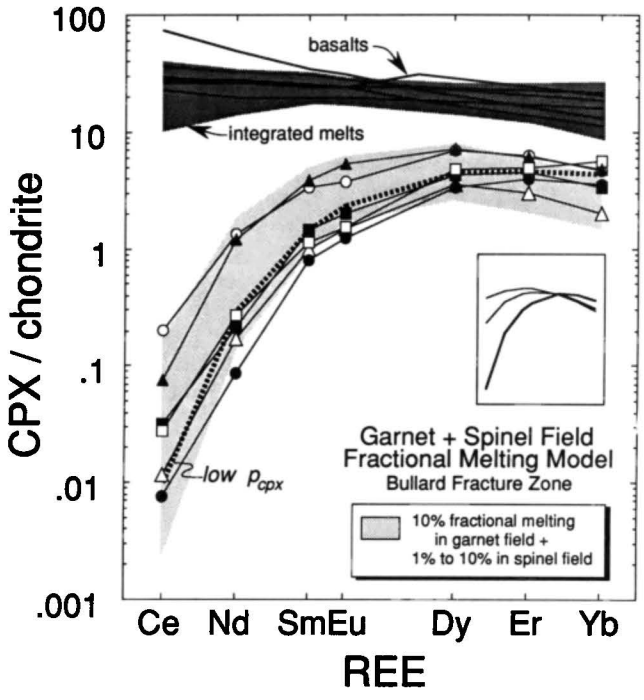

Fig. 13. Melting model in which melting in small increments begins in the garnet stability field (up to 10% total melting in the garnet field) and continues up to an additional 10% in the spinel stability field. Data from East and West Bullard FZ peridotite clinopyroxenes (symbols) conform to both the shape (Dy hump) and to the total degree of melting inferred from Ti-Zr model (Figure 9*a*). Spatially associated basalts [*leRoex et al.*, 1985] and two-stage integrated fractional liquids are also plotted. The dashed line is a residue model calculated using lower p_{cpx} in the melting assemblage (see text for discussion). The inset is a schematic representation of the evolution of the MREE hump in clinopyroxenes with melting from 1% (upper line) to 10% (bolder line) in the presence of garnet as discussed in the text. Symbols as in Figure 6.

a composition range encompassing spatially associated MORB from the Bullard Fracture Zone (Figure 13).

Discussion

Correlation between peridotite major element compositions and proximity to hotspots has recently been demonstrated [*Dick et al.*,1984; *Dick*, 1989]. Peridotites dredged from closest proximity to hotspots on the Southwest Indian and Mid-Atlantic ridges have higher modal olivine, higher Cr/(Cr+Al) in spinel, higher Mg # and lower Al_2O_3 in enstatite, and lower Na_2O in diopside compared to those dredged away from hotspots [*Dick et al.*, 1984; *Dick*, 1989]. The same relationship is reflected in the abundances of incompatible trace elements in clinopyroxenes (Figure 4) and in the inverse correlation between Mg # and Ce in cpx (Figure 3).

These observations are consistent with higher degrees of melting in the upper mantle nearest to hotspots. Thus it follows that chemically and isotopically enriched basalts erupted at mid-ocean ridges near hotspots [*Hart et al.*, 1973; *Schilling et al.*, 1983; *leRoex et al.*, 1983] are not related in a simple way to the spatially associated, highly depleted subridge upper mantle. While enriched basalts erupted near hotspot-ridge intersections may be produced by melting a heterogeneous mantle composed of incompatible element-depleted and -enriched components [*leRoex et al.*, 1983], it appears that the hotspot-proximal peridotites in the present data set represent the depleted component and have experienced the highest degrees of melting and depletion because of the hotspot influence. If hotspots impose higher ambient temperatures on the mantle, then melting would be more extensive and would begin deeper. This is consistent with the interpretation of modeling results that Bouvet FZ and Discovery II FZ peridotites experienced some melting in the garnet stability field. Some samples away from hotspots are consistent with melting in the spinel field alone since a slightly lower mantle temperature will result in initiation of melting at lower pressure, i.e., in the spinel stability field [*O'Hara et al.*, 1971; *McKenzie and Bickle*, 1988].

The influence of garnet in the melting assemblage is not restricted to hotspot areas. Based on modeling results and on the observed shape of REE patterns in Vulc 5: 34-56, 35-1, 35-19,and 37-3 from the Bullard FZ and on modeling results, melting in these samples commenced in the garnet stability field and continued into the spinel field up to ~17% total melting. Theoretical models for subridge melting and studies of alpine massifs also conclude that melting commences in the garnet field and does not exceed 25% [*Loubet et al.*, 1975; *Ahern and Turcotte*, 1979; *McKenzie*, 1984; *Nicolas*, 1986; *McKenzie and Bickle*, 1988]. Additional convincing support for the involvement of garnet in mid-ocean ridge basalt petrogenesis comes from a recent study of Hf and Nd isotopes in MORB [*Salters and Hart*, 1989] which concluded that the observed isotopic covariations are consistent with garnet in the source of ocean ridge basalts.

Of the samples that have experienced >15% melting based on Ti-Zr modeling, all but one are modeled by early melting in the garnet stability field. This implies that if total melting is >15% in a sample, then melting began in the garnet stability field. This has important thermal implications in light of recent theoretical models for melt generation at spreading centers [*McKenzie and Bickle*, 1988]. For melting to begin in the garnet stability field in the thermal environment proposed by *McKenzie and Bickle* [1988], the potential temperature of the mantle must be ~50°C hotter than the 1280°C they predict. Enhanced melting starting in the garnet field in the hotspot related samples may be explained by higher temperatures, but deeper melting away from hotspots may call for a different explanation. The model of *McKenzie and Bickle* [1988] would change if fractional, rather than batch, melting equations were used since the mantle solidus would increase with each fraction of melt extracted; *McKenzie and Bickle* [1988] themselves believe that batch melting is unrealistic. A more realistic model requires knowledge of latent heats of fusion at different pressures, the oceanic geothermal gradient, and changes in the mantle solidus with degree of depletion and fractional melt extraction. Since all of their assumptions of such parameters are based on available experimental petrology data, which are essentially batch melt compositions, a more realistic theoretical fractional or incremental melting model cannot be constructed at this time.

If melting beneath fracture zones is subdued relative to melting beneath ridge centers [*Fox et al.*, 1980; *Phipps Morgan and Forsyth*, 1988], then it is expected that the high degrees of melting we infer for hotspot-proximal peridotites sampled in fracture zones would be even higher beneath the ridge axis. It should also be noted that *Phipps Morgan and Forsyth* [1988] predicted on the basis of numerical experiments that melting should commence at deeper levels beneath fracture zones than beneath ridge centers. Our assertion that garnet was involved in the early melting history of some fracture zone abyssal peridotites lends support to their hypothesis, although we cannot at this point comment on the depths of melting at ridge centers.

LREE-enriched melts from an enriched component of the upper mantle or from melting in the garnet stability field might be responsible for the unusual REE and Sr abundances in IO11/76: 58-34 and Prot 5: 19-2 (Figure 7). The LREE inflections in these samples are probably not primary since they do not resemble the partitioning behavior of REE in any phase present in the samples. However, they could be evidence for a limited extent of interaction between the depleted peridotite and a LREE-enriched liquid. Worth noting is the similarity of our observed patterns in these samples and those predicted by *Navon and Stolper* [1987, Figure 4] for residual mantle undergoing metasomatism by incompatible element enriched melts. The fact that two separate volumes of mantle show nearly identical LREE anomalies implies that the process may be common under ocean ridges.

The mechanism creating negative HFSE anomalies in peridotite clinopyroxenes, but not in MORB, remains a puzzle. As *Salters and Shimizu* [1988] noted, basalts carrying many of the intraplate xenoliths do not show corresponding HFSE depletions, a characteristic observed and heretofore associated only with magmas formed above subduction zones in continental and island arcs. Most published cpx/liquid partition coefficients for REE, Ti and Zr do not exhibit negative Ti and Zr anomalies relative to adjacent REE in an incompatible element diagram sequence. Thus, if the source composition does not have HFSE anomalies, and if no phase in the residual assemblage preferentially partitions both Ti and Zr into its structure over REE, then melting will not produce negative HFSE anomalies in clinopyroxene and flat patterns in the derived liquids. The fact that samples from the Bouvet FZ, which are the most depleted in incompatible elements, also exhibit the largest negative HFSE anomalies, and that anomalies in less depleted samples from the Vulcan FZ (Vulc5: 41-13 and 41-15) are smaller than those in more depleted samples (Vulc5: 41-30 and 41-45; Figure 8) are both significant. Taken together, these observations imply that the anomalies grow with increasing degrees of melting, which in turn implies that $D_{Zr}^{cpx/liq}$ is lower than adjacent D_{REE}. Inspection of the melting equations in the appendix shows that a negative Zr anomaly of the observed magnitude can arise by decreasing P_{Zr} or D_o^{Zr}. This change can be effected by decreasing $D_{Zr}^{cpx/liq}$ from the "nonanomalous" value of 0.20 to a value of 0.17, a change well within the range of reported $D_{Zr}^{cpx/liq}$. Figure 8 also illustrates that Ti/Ti* does not decrease with increased melting and that most MORB have Zr/Zr* > 1.0 and Ti/Ti* < 1.0. This implies that Ti and Zr do not behave identically as is often assumed in discussions of HFSE. However, a model that accounts for the characteristic incompatible element patterns of both peridotite clinopyroxenes and MORB requires a better understanding of MORB source characteristics, of the partitioning of elements at different pressures in the upper mantle, and of the reactions between migrating melts and residues.

REE and Ti-Zr concentrations taken separately are consistent with a model of repeated melting and segregation of ≤0.1% increments, totaling from 5-25% melting, of a LREE-depleted (chondrite-normalized) source. Thus it appears that the melting process in nature approaches fractional fusion. Models that utilized increments of batch melting greater than 0.1% failed due to their inability to fractionate REE sufficiently to reproduce the data. Given uncertainties in the data and in the starting model parameters, melt increments may range from «0.1% to as much as 0.3%. Retention of «0.1% melt in the residue can occur (e.g., dynamic melting of *Langmuir et al.* [1977]), but greater amounts of retained melt will flatten the REE patterns and increase the incompatible element concentrations of residual peridotite clinopyroxenes. Because segregation occurs after ~0.1% melting in the present suite of samples, significant constraints are placed on the dynamic melting mechanism, and the implication is that melt removal is both rapid and efficient in the mid-ocean ridge upper mantle. Thus the results of this study can be used to constrain boundary conditions for theoretical geodynamical models of melt segregation, migration, and permeable flow in the subridge asthenosphere. The modeling results do not preclude the possibility that extensive degrees of melting occur at cusps corresponding to the garnet-spinel and spinel-plagioclase transitions in the peridotite solidus [*Presnall et al.*, 1979]. However, if melting does occur at a cusp in the solidus, the mechanisms controlling melt extraction and segregation from the residue must be fully operative to enable efficient melt removal.

Support for the fractional or small increment of melting model also comes from theoretical and experimental studies, field work in alpine massifs, and seismic studies of slow spreading ridges that indicate the amount of melt present in any portion of the subridge upper mantle is small and probably does not exceed 1-3% [*Beeré*, 1975; *Nisbet and Fowler*, 1978; *Ahern and Turcotte*, 1979; *Waff and Bulau*, 1979; *McKenzie*, 1984, 1985*a* and *b*; *Richter and McKenzie*, 1984; *Prinzhofer and Allègre*, 1985; *Nicolas*, 1986]. Further support comes from the depleted major element compositions of residual abyssal peridotites, which generally contain less than 1% primitive basaltic component. As these peridotites have undergone up to 25% melting, this demonstrates that melt removal is generally greater than 95% efficient in the shallow mantle [*Dick*, 1989], suggesting that little melt can be held in mantle peridotites during melting.

The observation that most oceanic peridotites retain primary diopside [*Dick and Fisher*, 1984] further supports the near-fractional melting model. Melting in the spinel stability field removes a cpx-rich liquid from the system leaving an increasingly olivine-opx-rich residue. Olivine has a higher enthalpy of fusion than do pyroxenes [*Robie et al.*, 1979], so removing diopside + pyroxene-rich liquid from the bulk system increases the heat required for melting to proceed from the four-phase (lherzolite) to the three-phase (cpx-free harzburgite) assemblage. This represents an effective thermodynamic barrier to melting beyond the cpx-out point if the liquid is efficiently removed. Interestingly, the only samples that might have moved from the four-phase to the three-phase field by loss of cpx are those from near the hotspots. This may be caused either by higher temperatures associated with hotspots or by possible lowering of solidus temperatures by water at hotspots [*Schilling et al.*, 1983]. This situation compares with alpine peridotite genesis wherein cpx-free harzburgites are evidence of enhanced, probably hydrous, melting [*Dick*, 1977; *Dick and Fisher*, 1984].

It might be expected that extremely depleted late stage fractional melts should rarely be sampled on the ridge system. No voluminous outpourings of such melts are expected and indeed none have been found, but extremely depleted Mg-rich silicate melt inclusions have been found in olivine and plagioclase xenocrysts in MORB from the Galapagos spreading center [*Yonover*, 1989], and from various locations on the Mid-Atlantic Ridge and Iceland [*Sobolev and Dmitriev*, 1989; K. Johnson, manuscript in preparation, 1990]. Ongoing examination of melt inclusions from the Mid-Atlantic Ridge, the American-Antartica Ridge, and the Southwest Indian Ridge should provide additional data to address this question.

Compatible major elements in basaltic melts are buffered by the major peridotite phases and will show little variation as they

emerge from the top of the melting column [*Richter*, 1986; *Navon and Stolper*, 1987; *Dick*, 1989]. This, in conjunction with aggregation and mixing of melts in a magma chamber, will obfuscate the melting process recorded in basalts making fractional melting and melt integration difficult to distinguish from batch melting when looking at basalt compositions. Therefore the liquids erupted at the surface as MORB are weighted averages of melts produced over the melting interval and do not show a simple batch melting relationship to the latest stage residues of melting sampled as abyssal peridotites.

Conclusions

Several important conclusions can be made in this study.

1. Both major and incompatible trace elements in abyssal peridotites reflect greater degrees of melting in the upper mantle near the Bouvet and Marion hotspots. Furthermore, pronounced chemical gradients in the upper mantle approaching hotspots are manifested in peridotite clinopyroxene compositions.

2. Negative anomalies in Zr and Ti (HFSE anomalies) are observed in abyssal peridotite clinopyroxenes. The Zr anomalies are greatest near the Bouvet hotspot and appear to increase with increasing depletion of the samples, or with increasing degree of melting. Ti anomalies do not exhibit this systematic behavior. Thus partition coefficients for Zr in cpx may be lower than adjacent elements in incompatible element diagrams (spidergrams). However, processes relating the observed negative Zr anomalies in peridotite cpx to positive anomalies in MORB are still not clear.

3. Ti, Zr, and REE concentrations in abyssal peridotite cpx are best modeled by fractional melting or by melting and segregation in ≤ 0.1% increments. Some REE patterns are consistent with melting in the spinel stability field alone (Vulcan FZ, Atlantis II FZ), others are consistent with varying degrees of melting beginning in the garnet stability field and continuing into the spinel field (Bullard FZ), while those near hotspots (Bouvet and Discovery II FZs) are consistent with melting and recrystallization of a garnet-bearing assemblage and subsequent granule exsolution of clinopyroxene from orthopyroxene. Near-fractional melting and melting beginning in the garnet stability field place constraints on models for MORB generation and theoretically based concepts of melt segregation and subridge thermal structure.

4. The melting model is consistent with theoretical, experimental, geophysical, and on-land observations stating that only very small fractions of melt are needed before segregation can commence and that essentially no trapped liquid remains in the residue after segregation and compaction [*Ahern and Turcotte*, 1978; *McKenzie*, 1984; *Nicolas*, 1986; *McKenzie and Bickle*, 1988; *Dick*, 1989].

The implications of this study are that "common" MORB is evolved from a weighted aggregate of very small increments of melting produced over a depth range often beginning in the garnet stability field.

Appendix

Basic melting equations derived by *Gast* [1968] and *Shaw* [1970] are recast to describe the change in concentration of an element in cpx with melting.

Assumptions

A $D_i\alpha = \dfrac{C_i\alpha}{C_i^l} \equiv \dfrac{\text{concentration of element } i \text{ in phase } \alpha}{\text{concentration of element } i \text{ in liquid}} \equiv \text{const}$

B $D_i^{\alpha/cpx} = \dfrac{C_i\alpha}{C_i^{cpx}} \equiv \dfrac{\text{concentration of element } i \text{ in phase } \alpha}{\text{concentration of element } i \text{ in cpx}} \equiv \text{const}$

C $X_{o,\alpha} \equiv$ initial weight fraction of phase α

D $C_i^s \equiv$ concentration of i in bulk solid;
$C_i^l \equiv$ concentration of i in liquid;
$C_i^o \equiv$ concentration of i in original bulk solid

E F is degree of melting.

F nonmodal melting of prescribed mineral proportions

$D_i^o = \Sigma D_i\alpha X_{o,\alpha} \equiv$ initial bulk solid partition coefficient of element i. (A1)

$P = \Sigma D_i\alpha p_\alpha \equiv$ weighted partition coefficient of liquid; $p\alpha =$ proportion of mineral phase entering liquid. (A2)

$D_i = \Sigma D_i\alpha X_\alpha = (D_i^o - PF) / (1 - F) \equiv$ bulk solid partition coefficient of element i at F percent melting. (A3)

G Equilibrium maintained between all phases.

H All garnet remaining after melting in the garnet stability field

TABLE A1. Crystal/Liquid Partition Coefficients Used in Models

	Olivine	Cinopyroxene	Orthopyroxene	Garnet	Spinel	Plagioclase
Ti	0.02	0.44	0.10	0.6	0.10	0.01
Zr	0.01	0.20	0.05	0.5	0.05	0.01
Ce	0.001	0.10	0.005	0.008	0.0005	
Nd	0.002	0.19	0.01	0.057	0.0008	
Sm	0.003	0.30	0.02	0.217	0.0009	
Eu	0.003	0.42	0.03	0.45	0.0009	
Dy	0.012	0.50	0.045	2.0	0.0015	
Er	0.025	0.51	0.06	3.5	0.003	
Yb	0.059	0.50	0.075	7.0	0.0045	

Sources of data: Clinopyroxene: REE, *Irving and Frey* [1984], *Green and Pearson* [1985], *Johnson and Kinzler* [1989]. Ti, Zr, *McCallum and Charrette* [1978], *Fujimaki et al.* [1984], *Dunn* [1987], *Tormey et al.* [1987], *Johnson and Kinzler* [1989]. Olivine, opx: REE, *Stosch* [1982], combined with cpx partition coefficients. Ti, Zr, *Fujimaki et al.* [1984]. Spinel: REE, *Stosch* [1982], combined with cpx partition coefficients. Ti, Zr, K. Johnson, Ti calculated from electron probe data; Zr estimated from secondary ion counts relative to cpx. Garnet: REE, *Shimizu and Kushiro* [1975], *Nicholls and Harris* [1980], *Fujimaki et al.* [1984]. Ti, Zr, *Fujimaki et al.* [1984], *Green et al.* [1989]. Plagioclase: Zr - *Fujimaki et al.* [1984].

TABLE A2. Phase Proportions Used in the Models

Phase	Starting mode (Vol %)	Melt mode (Vol%)
olivine	0.55	0.10
opx	0.25	0.20
cpx	0.18	0.68
spinel	0.02	0.02
	High p_{cpx}	
olivine	0.55	0.03
opx	0.20	0.03
cpx	0.15	0.44
garnet	0.10	0.50
	Low p_{cpx}	
olivine	0.55	0.13
opx	0.20	0.12
cpx	0.15	0.25
garnet	0.10	0.50

reacts to form 2.5 enstatite + 0.75 diopside + 1.0 spinel upon ascent into the spinel stability field

Given

Fractional Melting

$$\frac{C_i^s}{C_i^o}=\left[\frac{1}{1-F}\right]\left[1-\frac{PF}{D_i^o}\right]^{\frac{1}{P}}$$

Equilibrium Batch Melting

$$\frac{C_i^s}{C_i^o}=\left[\frac{D_i^o-PF}{1-F}\right]\left[\frac{1}{D_i^o+F\ (1-P\ )}\right]$$

and knowing that $\frac{C_i{}^s}{C_i{}^o}$ can also be expressed as

$$\frac{(X_{ol}C_i{}^{ol}+X_{opx}C_i{}^{opx}+X_{cpx}C_i{}^{cpx}+X_{sp}C_i{}^{sp})}{(X_{o,ol}C_i{}^{o,ol}+X_{o,opx}C_i{}^{o,opx}+X_{o,cpx}C_i{}^{o,cpx}+X_{o,sp}C_i{}^{o,sp})}$$

which can be rewritten (by introducing $C_i{}^l$ and $C_i{}^{o,l}$, assuming $X_{ol}C_i{}^{ol}=X_{ol}\frac{C_i{}^{ol}}{C_i{}^l}\cdot\frac{C_i{}^l}{C_i{}^{cpx}}\cdot C_i{}^{cpx}$, etc., and then pulling out $C_i{}^{cpx}$ and $C_i{}^{o,cpx}$) as

$$\left[\frac{\frac{C_i{}^{cpx}\cdot C_i{}^l}{C_i{}^{cpx}}}{\frac{C_i{}^{o,cpx}\cdot C_i{}^{o,l}}{C_i{}^{o,cpx}}}\right]\ \mathbf{X}$$

$$\frac{\left(X_{ol}\frac{C_i{}^{ol}}{C_i{}^l}+X_{opx}\frac{C_i{}^{opx}}{C_i{}^l}+X_{cpx}\frac{C_i{}^{cpx}}{C_i{}^l}+X_{sp}\frac{C_i{}^{sp}}{C_i{}^l}\right)}{\left(X_{o,ol}\frac{C_i{}^{o,ol}}{C_i{}^{o,l}}+X_{o,opx}\frac{C_i{}^{o,opx}}{C_i{}^{o,l}}+X_{o,cpx}\frac{C_i{}^{o,cpx}}{C_i{}^{o,l}}+X_{o,sp}\frac{C_i{}^{o,sp}}{C_i{}^{o,l}}\right)}$$

the numerator and denominator of the second term are D_i and $D_i{}^o$, respectively, so that

$$\frac{C_i{}^s}{C_i{}^o}=\frac{C_i{}^{cpx}}{C_i{}^{o,cpx}}\cdot\left[\frac{\frac{C_i{}^l}{C_i{}^{cpx}}}{\frac{C_i{}^{o,l}}{C_i{}^{o,cpx}}}\right]\cdot\frac{D_i}{D_i{}^o}$$

Applying assumption A above yields

$$\frac{C_i{}^s}{C_i{}^o}=\frac{C_i{}^{cpx}}{C_i{}^{o,cpx}}\cdot\frac{D_i}{D_i{}^o}$$

and then equating this with expressions for fractional and batch melting from *Shaw* [1970], we get

fractional

$$\frac{C_i^s}{C_i^o}=\frac{C_i{}^{cpx}}{C_i{}^{o,cpx}}\cdot\frac{D_i}{D_i^o}=\left[\frac{1}{1-F}\right]\left[1-\frac{PF}{D_i^o}\right]^{\frac{1}{P}}$$

batch

$$\frac{C_i^s}{C_i^o}=\frac{C_i{}^{cpx}}{C_i{}^{o,cpx}}\cdot\frac{D_i}{D_i^o}=\left[\frac{D_i^o-PF}{1-F}\right]\left[\frac{1}{D_i^o+F\ (1-P\ )}\right]$$

D_i is given in assumption (A3) above (*Shaw* [1970], equation 12), and by substitution the whole rock equations can be rewritten in terms of $C_i{}^{cpx}/C_i{}^{o,cpx}$ or $C_i{}^{cpx}/C_i{}^o$

Fractional melting

$$\frac{C_i{}^{cpx}}{C_i{}^{o,cpx}}=\left[1-\frac{PF}{D_i^o}\right]^{\left(\frac{1}{P}-1\right)} \tag{A4}$$

or

$$\frac{C_i{}^{cpx}}{C_i{}^o}=\left[1-\frac{PF}{D_i{}^o}\right]^{\frac{1}{P}}\cdot\left[\frac{D_i{}^{cpx/l}}{D_i{}^o-PF}\right] \tag{A5}$$

Batch melting

$$\frac{C_i{}^{cpx}}{C_i{}^{o,cpx}}=\left[\frac{D_i^o}{D_i^o+F\ (1-P\ )}\right] \tag{A6}$$

or

$$\frac{C_i{}^{cpx}}{C_i{}^o}=\left[\frac{D_i{}^{cpx/l}}{D_i^o+F\ (1-P\ )}\right] \tag{A7}$$

Acknowledgements. Many of the samples analyzed in this study were made available by R. L. Fisher of Scripps Institution of Oceanography, who is gratefully acknowledged. Also aiding in the collection of samples were Beecher Wooding, Hugh Bergh, and Anton leRoex. Samples for ion probe partitioning studies were provided by Tim Grove and Ro Kinzler at MIT. We are grateful to Ken Burrhus, who kept the ion probe in perfect working order and to the captains and crews of R/Vs *Melville*, *Atlantis* II, *Islas Orcadas*, *Robert D. Conrad*, and *PolarStern*. Discussions with Stan Hart, Fred Frey, Peter Kelemen, Dan McKenzie, Peter Meyer, and Rob Yonover were helpful. Careful reviews by Stan Hart, Fred Frey, Bill Bryan, Peter Michael and an anonymous reviewer greatly improved the manuscript. We thank Steve DeLong for carefully checking the derivations in the appendix. Funding was provided by WHOI Ocean Ventures Fund (K.J.), NSF-DPP-8720002 and NSF-OCE-8416634 to H.J.B.D., NSF-EAR-8419832 and NSF-EAR-8805221 to N. S. WHOI contribution no. 7211.

REFERENCES

Ahern, J. L., and D. L. Turcotte, Magma migration beneath an ocean ridge, *Earth Planet. Sci. Lett., 45*, 115-122, 1979.

Anders, E., and M. Ebihara, Solar-system abundances of the elements, *Geochim. Cosmochim. Acta, 46*, 2363-2380, 1982.

Beeré, W., A unifying theory of the stability of penetrating liquid phases and sintering pores, *Acta Metall., 23*, 131-138, 1975.

Bender, J. F., C. H. Langmuir, and G. N. Hanson, Petrogenesis of basalt glasses from the Tamayo region, East Pacific Rise, *J. Petrol., 25*, 213-254, 1984.

Bottinga, Y., and C. J. Allègre, Partial melting under spreading ridges, *Philos. Trans. R. Soc. London, Ser. A., 288*, 501-525, 1978.

Colson, R. O., and D. Gust, Effects of pressure on partitioning of trace elements between low-Ca pyroxene and melt, *Am. Mineral., 74*, 31-36, 1989.

Davis, B. T. C., and J. F. Shairer, Melting relations in the join diopside-forsterite-pyrope at 40 kbars and at one atmosphere, *Yearbook Carnegie Inst. Washington, 64*, 123-126, 1965.

Dick, H. J. B., Partial melting in the Josephine Peridotite, I, the effect on mineral composition and its consequence for geobarometry and geothermometry, *Am. J. Sci., 277*, 801-832, 1977.

Dick, H. J. B., Abyssal peridotites, very-slow spreading ridges and ocean ridge magmatism, in *Magmatism in the Ocean Basins*, edited by A. D. Saunders and M. J. Norry, pp. 71-105, Geol. Soc. London Spec. Pub. No. 42, 1989.

Dick, H. J. B. and R. L. Fisher, Mineralogic studies of the residues of mantle melting: abyssal and alpine-type peridotites, in *Kimberlites II: The Mantle and Crust Relationships*, edited by J. Komprobst, pp. 295-308, Elsevier, New York, 1984.

Dick, H. J. B., R. L. Fisher, and W. B. Bryan, Mineralogic variability of the uppermost mantle along mid-ocean ridges, *Earth Planet. Sci. Lett., 69*, 88-106, 1984.

Dunn, T., Partitioning of Hf, Lu, Ti, and Mn between olivine, clinopyroxene and basaltic liquid, *Contrib. Mineral. Petrol., 96*, 476-484, 1987.

Elthon, D., and C. M. Scarfe, High-pressure phase equilibria of a high-magnesia basalt and the genesis of primary oceanic basalts, *Am. Mineral., 69*, 1-15, 1984.

Falloon, T. J., and D. H. Green, Anhydrous partial melting of MORB pyrolite and other peridotite compositions at 10 kbar: implications for the origin of primitive MORB glasses, *Mineral. and Petrol., 37*, 181-219, 1987.

Falloon, T. J., and D. H. Green, Anhydrous partial melting of a fertile and depleted peridotite from 2 to 30 kb and application to basalt petrogenesis, *J. Petrol., 29*, 1257-1282, 1988.

Fisher, R. L., H. J. B. Dick, J. H. Natland, and P. S. Meyer, Mafic/ultramafic suites of the slowly spreading Southwest Indian Ridge: Protea exploration of the Antarctic plate boundary, 24°E-47°E, 1984, *Ofioliti, 11*, 147-178, 1987.

Fox, P. J., R. S. Detrick, and G. M. Purdy, Evidence for crustal thinning near fracture zones: implications for ophiolites, in *Ophiolites, Proceedings International Ophiolite Symposium, Cyprus, 1979*, edited by A. Panayiotou, pp. 161-168, Ministry of Agriculture and Natural Resources, Nicosia, Cyprus, 1980.

Frey, F. A., C. J. Suen, and H. W. Stockman, The Ronda high temperature peridotite: Geochemistry and petrogenesis, *Geochim. Cosmochim. Acta, 49*, 2469-2491, 1985.

Fujii, T., and C. M. Scarfe, Compositions of liquids coexisting with spinel lherzolite at 10 kbar and the genesis of MORBs, *Contrib. Mineral. Petrol., 90*, 18-28, 1985.

Fujimaki., H., M. Tatsumoto, and K. Aoki, Partition coefficients of Hf, Zr, and REE between phenocrysts and groundmass, *Proc. Lunar Planet. Sci. Conf., 14th, Part 2, J. Geophys. Res., 89*, suppl., B662-B672, 1984.

Gast, P. W., Trace element fractionation and the origin of tholeiitic and alkaline magma types, *Geochim. Cosmochim. Acta, 32*, 1057-1086, 1968.

Green, D. H., and A. E. Ringwood, The genesis of basaltic magmas, *Contrib. Mineral. Petrol., 15*, 103-190, 1967.

Green, D. H., W. O. Hibberson, and A. L. Jaques, Petrogenesis of mid-ocean ridge basalts, in *The Earth:Its Origin, Structure, and Evolution*, edited by M. W. McElhinney, pp. 265-299, Academic Press, San Diego, Calif., 1979.

Green, T. H., and N. J. Pearson, Rare earth element partitioning between clinopyroxene and silicate liquid at moderate to high pressure, *Contrib. Mineral. Petrol., 91*, 24-36, 1985.

Green, T. H., S. H. Sie, C. G. Ryan, and D. R. Cousens, Proton microprobe-determined partitioning of Nb, Ta, Zr, Sr, and Y between garnet, clinopyroxene and basaltic magma at high pressure and temperature, *Chem. Geol., 74*, 201-216, 1989.

Grutzeck, M., S. Kridelbaugh, and D. Weill, The distribution of Sr and REE between diopside and silicate liquid, *Geophys. Res. Lett., 1*, 273-275, 1974.

Hart, S. R., J.-G. Schilling, and J. L. Powell, Basalts from Iceland and along the Reykjanes Ridge: Sr isotope geochemistry, *Nature Phys. Sci., 246*, 104, 1973.

Hofmann, A. W., and M. D. Feigenson, Case studies on the origin of basalt, I, Theory and reassessment of Grenada basalts, *Contrib. Mineral. Petrol., 84*, 382-389, 1983.

Humphris, S. E., G. Thompson, J.-G. Schilling, and R. H. Kingsley, Petrological and geochemical variations along the Mid-Atlantic Ridge between 46°S and 32°S: Influence of the Tristan da Cunha mantle plume, *Geochim. Cosmochim. Acta, 49*, 1445-1464, 1985.

Irving, A. J. and F. A. Frey, Trace element abundances in megacrysts and their host basalts: Constraints on partition coefficients and megacryst genesis, *Geochim. Cosmochim. Acta, 48*, 1201-1221, 1984.

Jaques, A. L., and D. H. Green, Anhydrous melting of peridotite at 0-15 kbar pressure and the genesis of tholeiitic basalts, *Contrib. Mineral. Petrol., 73*, 287-310, 1980.

Johnson, K. T. M., and R. J. Kinzler, Partitioning of REE, Ti, Zr, Hf, and Nb between clinopyroxene and basaltic liquid: An ion microprobe study, *Eos Trans. AGU, 70*, 1388, 1989.

Johnson, K. T. M., H. J. B. Dick, and N. Shimizu, Rare earth element composition of discrete diopsides from the oceanic upper mantle: Implications for MORB genesis and processes of exotic melt infiltration, *Eos Trans. AGU, 68*, 1541, 1987.

Johnson, K. T. M., H. J. B. Dick, and N. Shimizu, Trace element composition of diopsides in abyssal peridotites: Implications for generation of mid-ocean ridge basalts, *Eos Trans. AGU, 69*, 1516, 1988.

Kay, R. W., N. J. Hubbard, and P. W. Gast, Chemical characteristics and origin of ocean ridge volcanic rocks, *J. Geophys. Res., 75*, 1585-1613, 1970.

Klein, E. M., and C. H. Langmuir, Global Correlations of ocean ridge basalt chemistry with axial depth and crustal thickness, *J. Geophys. Res., 92*, 8089-8115, 1987.

Langmuir, C. H., J. F. Bender, A. E. Bence, G. N. Hanson, and S. R. Taylor, Petrogenesis of basalts from the FAMOUS area: Mid-Atlantic Ridge, *Earth Planet. Sci. Lett., 36*, 133-156, 1977.

Lawver, L. A., and H. J. B. Dick, The American-Antarctic Ridge, *J. Geophys. Res., 88*, 8193-8202, 1983.

le Pichon, X., J. Angelier, and J. C. Sibuet, Plate boundaries and extensional tectonics, *Tectonophysics, 81*, 239-256, 1982.

leRoex, A. P., H. J. B. Dick, A. J. Erlank, A. M. Reid, F. A. Frey, and S. R. Hart, Geochemistry, mineralogy, and petrogenesis, of lavas erupted along the Southwest Indian Ridge between the Bouvet triple junction and 11 degrees east, *J. Petrol., 24*, 267-318, 1983.

leRoex, A. P., H. J. B. Dick, and R. L. Fisher, Petrology and geochemistry of MORB from 25°E to 46°E along the Southwest Indian Ridge: Evidence for contrasting styles of mantle enrichment, *J. Petrol., 30*, 947-986, 1989.

Lindsley, D. H. and D. J. Andersen, A two-pyroxene thermometer, *Proc. Lunar Planet. Sci. Conf., 13th, Part 2, J. Geophys. Res., 88*, suppl., A887-A906, 1983.

Loubet, M., N. Shimizu, and C. J. Allègre, Rare earth elements in alpine peridotites, *Contrib. Mineral. Petrol., 53*, 1-12, 1975.

McCallum, I. S., and M. P. Charette, Zr and Nb partition coefficients: implications for the genesis of mare basalts, KREEP, and sea floor basalts, *Geochim. Cosmochim. Acta, 42*, 859-869, 1978.

McKenzie, D., The generation and compaction of partially molten rock, *J. Petrol., 25*, 713-765, 1984.

McKenzie, D., ^{230}Th-^{238}U disequilibrium and the melting processes beneath ridge axes, *Earth Planet. Sci. Lett., 72*, 149-157, 1985*a*.

McKenzie, D., The extraction of magma from the crust and mantle, *Earth Planet. Sci. Lett., 74*, 81-91, 1985*b*.

McKenzie, D., and M. J. Bickle, The volume and composition of melt generated by extension of the lithosphere, *J. Petrol., 29*, 625-679, 1988.

Michael, P. J., and E. Bonatti, Peridotite composition from the North Atlantic: Regional and tectonic variations and implications for partial melting, *Earth Planet. Sci. Lett., 73*, 91-104, 1985.

Minster, J. F., and C. J. Allègre, Systematic use of trace elements in igneous processes, III, Inverse problem of batch partial melting in volcanic suites, *Contrib. Mineral. Petrol., 68*, 37-52, 1978.

Morgan, W. J., Deep mantle convection plumes and plate motions, *Am. Assoc. Pet. Geol. Bull., 56*, 203-213, 1972.

Mysen, B. O., and I. Kushiro, Compositional variations of co-existing phases with degree of melting of peridotite in the upper mantle, *Am. Mineral., 62*, 843-865, 1977.

Navon, O., and E. Stolper, Geochemical consequences of melt percolation: The upper mantle as a chromatographic column, *J. Geol., 95*, 285-308, 1987.

Nicholls, I. A., and K. L. Harris, Experimental rare earth element partition coefficients for garnet, clinopyroxene, and amphibole coexisting with andesitic and baslatic liquids, *Geochim. Cosmochim. Acta, 44*, 287-308, 1980.

Nicolas, A., A melt extraction model based on structural studies in mantle peridotites, *J. Petrol., 27*, 999-1022, 1986.

Nisbet, E. G., and C. M. R. Fowler, The Mid-Atlantic Ridge at 37° and 45°N: Some geophysical and petrological constraints, *Geophys. J. R. Astron. Soc., 54*, 631-660, 1978.

O'Hara, M. J., Are ocean floor basalts primary magma?, *Nature, 220*, 683-686, 1968.

O'Hara, M. J., and H. S. Yoder, Jr., Formation and fractionation of basic magmas at high pressures, *Scott. J. Geol., 3*, 67-117, 1967.

O'Hara, M. J., S. W. Richardson, and G. Wilson, Garnet-peridotite stability and occurrence in the crust and mantle, *Contrib. Mineral. Petrol., 32*, 48-68, 1971.

O'Nions, R. K., and R. J. Pankhurst, Petrogenetic significance of isotope and trace element variations in volcanics from the Mid-Atlantic, *J. Petrol., 15*, 603-634, 1974.

Phipps Morgan, J., and D. W. Forsyth, Three-dimensional flow and temperature perturbations due to a transform offset: Effects on Oceanic crustal and upper mantle structure, *J. Geophys. Res., 93*, 2955-2966, 1988.

Presnall, D. C., and J. D. Hoover, High pressure phase equilibrium constraints on the origin of mid-ocean ridge basalts, *Magmatic Processes: Physicochemical Principles*, edited by B. O. Mysen, pp. 75-89, Spec. Publ., The Geochem. Soc., 1, 1987.

Presnall, D. C., J. R. Dixon, T. H. O'Donnell, and S. A. Dixon, Generation of mid-ocean ridge tholeiites, *J. Petrol., 20*, 3-35, 1979.

Prinzhofer, A., and C. J. Allègre, Residual peridotites and the mechanisms of partial melting, *Earth Planet. Sci. Lett., 74*, 251-265, 1985.

Ray, G. L., N. Shimizu, and S. R. Hart, An ion microprobe study of the partitioning of trace elements between clinopyroxene and liquid in the system diopside-albite-anorthite, *Geochim. Cosmochim. Acta, 47*, 2131-2140, 1983.

Richter, F. M., Simple models for trace element fractionation during melt segregation, *Earth Planet. Sci. Lett., 77*, 333-344,1986.

Richter, F. M., and D. McKenzie, Dynamical models for melt segregation from a deformable matrix, *J. Geol., 92*, 729-740, 1984.

Robie, R. A., B. S. Hemingway, and J. R. Fisher, Thermodynamic properties of minerals and related substances at 298.15 K and 1 bar (105 pascals) pressure and at higher temperatures, *U.S. Geol. Surv. Bull., 1452*, 456 pp., 1979.

Rouffosse, M., B. Parsons, D. McKenzie, and T. Watts, Geoid and depth anomalies in the Indian Ocean, *Eos Trans. AGU, 62*, 389, 1981.

Salters, V. J. M., and S. R. Hart, The Hf-paradox and the role of garnet in the source of mid-ocean ridge basalts, *Nature, 342*, 420-422, 1989.

Salters, V. J. M., and N. Shimizu, World-wide occurrence of HFSE-depleted mantle, *Geochim. Cosmochim. Acta, 52*, 2177-2182, 1988.

Schilling, J.-G., Rare earth variations across 'normal' segments of the Reykjanes Ridge, 60°-53°N, Mid-Atlantic Ridge, 29°S, and East Pacific Rise, 2°-19°S, and evidence on the composition of the underlying low-velocity layer, *J. Geophys. Res., 80*, 1459-1473, 1975.

Schilling, J.-G., M. Zajac, R. Evans, T. Johnston, W. White, J. D. Devine, and R. Kingsley, Petrologic and geochemical variations along the Mid-Atlantic Ridge from 29°N to 73°N, *Am. J. Sci., 283*, 510-586, 1983.

Sclater, J. G., C. Bowin, R. Hey, H. Haskins, J. Peirce, J. Phillips, and C. Tapscott, The Bouvet Triple Junction, J. *Geophys. Res., 81*, 1857-1869, 1976.

Shaw, D. M., Trace element fractionation during anatexis, *Geochim. Cosmochim. Acta, 34*, 237-243, 1970.

Shaw, D. M., Trace element behaviour during anatexis, Proceedings of Chapman Conference, Partial Melting in the Earth's Upper Mantle, edited by H. J. B Dick, *Bull. Oreg. Dep. Geol. Miner. Ind., 96*, 189-213, 1977.

Shibata, T., and G. Thompson, Peridotites from the Mid-Atlantic Ridge at 43°N and their petrogenetic relation to abyssal tholeiites, *Contrib. Mineral. Petrol., 93*, 144-159, 1986.

Shibata, T., G. Thompson, and F. A. Frey, Tholeiitic and alkali basalts from the Mid-Atlantic Ridge at 43°N, *Contrib. Mineral. Petrol., 70*, 127-141, 1979.

Shimizu, N., and S. R. Hart, Rare earth element concentrations in clinopyroxenes from an ocean-ridge lherzolite, *Year Book Carnegie Inst. Washington, 73*, 964-967, 1974.

Shimizu, N., and I. Kushiro, The partitioning of rare earth elements between garnet and liquid at high pressures: Preliminary experiments, *Geophys. Res. Lett., 2*, 413-416, 1975.

Shimizu, N., M. P. Semet, and C. J. Allègre, Geochemical applications of quantitative ion-microprobe analysis, *Geochim. Cosmochim. Acta, 42*, 1321-1334, 1978.

Sobolev, A. V., and L. V. Dmitriev, Primary melts of tholeiites of oceanic rifts (TOR): Evidence from studies of primitive glasses and melt inclusions in minerals, paper presented at International Geological Congress, Washington, D.C., 1989.

Stolper, E., A phase diagram for mid-ocean ridge basalts: Preliminary results and implications for petrogenesis, *Contrib. Mineral. Petrol., 74*, 13-27, 1980.

Stosch, H.-G., Rare earth element partitioning between minerals from anhydrous spinel peridotite xenoliths, *Geochim. Cosmochim. Acta, 46*, 793-811, 1982.

Sun, S.-S., R. W. Nesbitt, and A. Y. Sharaskin, Geochemical characteristics of mid-ocean ridge basalts, *Earth Planet. Sci. Lett., 44*, 119-138, 1979.

Takahashi, E., and I. Kushiro, Melting of a dry peridotite at high pressures and basalt magma genesis, *Am. Mineral., 68*, 859-879, 1983.

Terakado, Y., and A. Masuda, Experimental study of REE partitioning between diopside and melt under atmospheric pressure, *Geochem. J., 13*, 121-129, 1979.

Tormey, D. R., T. L. Grove, and W. B. Bryan, Experimental petrology of normal MORB near the Kane Fracture Zone: 22°-25°N, Mid-Atlantic Ridge, *Contrib. Mineral. Petrol., 96*, 121-139, 1987.

Waff, H. S., and J. R. Bulau, Equilibrium fluid distribution in an ultramafic partial melt under hydrostatic stress conditions, *J. Geophys. Res., 84*, 6109-6114, 1979.

Yonover, R., Petrological effects of rift failure at the Galapagos Spreading Center near 95.5°W including analyses of glass inclusions by laser mass spectrometry and ion microprobe, PhD thesis, 193 pp., Univ. of Hawaii, May 1989.

H. J. B. Dick, 214 McLean Lab, Woods Hole Oceanographic Institution, Woods Hole, MA 02543.

K. T. M. Johnson, 224 Clark Lab, Woods Hole Oceanographic Institution, Woods Hole, MA 02543.

N. Shimizu, Woods Hole Oceanographic Institution, Woods Hole, MA 02543.

(Received May 16, 1989;
revised October 8, 1989;
accepted October 26, 1989)